Revision 1, Final published paper:

Scicchitano MR, Jollands MC, Williams IS, Hermann J, Rubatto D, Kita NT, Nachlas WO, Valley JW, Escrig S, Meibom A (2022) Oxygen diffusion in garnet: experimental calibration and implications for timescales of metamorphic processes and retention of primary O isotopic signatures. Am. Mineral. 107:1425-1441. DOI: https://doi.org/10.2138/am-2022-7970

Oxygen diffusion in garnet: experimental calibration and implications for timescales of metamorphic processes and retention of primary O isotopic signatures

Maria Rosa Scicchitano[1,2,‡,*], Michael C. Jollands[2,3], Ian S. Williams[2], Jörg Hermann[2,4], Daniela Rubatto[2,4,5], Noriko T. Kita[1], William O. Nachlas[1], John W. Valley[1], Stéphane Escrig[6], Anders Meibom[5,6]

[1] Department of Geoscience, University of Wisconsin-Madison, 53706 Madison, WI, USA (noriko@geology.wisc.edu; nachlas@wisc.edu; valley@geology.wisc.edu)

[2] Research School of Earth Sciences, Australian National University, Canberra 2601 ACT, Australia (ian.williams@anu.edu.au)

[3] Department of Earth and Environmental Sciences, Lamont Doherty Earth Observatory, Columbia University, Palisades, NY 10964, USA (jollands@ldeo.columbia.edu)

[4] Institute of Geological Sciences, University of Bern, 3012 Bern, Switzerland (daniela.rubatto@geo.unibe.ch; joerg.hermann@geo.unibe.ch)

[5] Institute of Earth Sciences, University of Lausanne, 1015 Lausanne, Switzerland

[6] Laboratory for Biological Geochemistry, Ecole Polytechnique Fédérale de Lausanne (EPFL), 1015 Lausanne, Switzerland (stephane.escrig@epfl.ch, anders.meibom@epfl.ch)

[‡] Present address: Deutsches GeoForschungsZentrum GFZ, D14473 Potsdam, Germany

* Corresponding author. E-mail: maria.rosa.scicchitano@gfz-potsdam.de

ABSTRACT

Knowledge of oxygen diffusion in garnet is crucial for a correct interpretation of oxygen isotope signatures in natural samples. A series of experiments was undertaken to determine the diffusivity of oxygen in garnet, which remains poorly constrained. Firstly, high-pressure (HP) nominally dry experiments were performed in piston cylinder apparatus at (i) T = 1050-1600 °C (P = 1.5 GPa) and (ii) T = 1500 °C (P = 2.5 GPa). In these, yttrium aluminum garnet (YAG; $Y_3Al_5O_{12}$) cubes were annealed in graphite powder mixed with fine-grained ^{18}O-enriched YAG + corundum (Crn) powder. Secondly, HP H_2O-saturated experiments were conducted at T = 900 °C and P = 1.0-1.5 GPa, wherein YAG crystals were packed into a YAG + Crn powder, along with ^{18}O-enriched H_2O. Thirdly, 1-atm experiments (YAG cubes coated with ^{18}O-enriched YAG and Crn powder) were performed in a gas-mixing furnace at T = 1500-1600 °C under Ar flux, to limit ^{18}O loss. Finally, an experiment at T = 900 °C (P = 1.0 GPa) was done using a pyrope cube embedded into pyrope powder and ^{18}O-enriched H_2O. Experiments using grossular were not successful.

Profiles of $^{18}O/(^{18}O+^{16}O)$ in the experimental charges were analyzed with three different Secondary Ion Mass Spectrometers (SIMS): Sensitive High Resolution Ion Microprobe (SHRIMP II and SI), CAMECA IMS-1280 and NanoSIMS. Considering only the measured length of ^{18}O diffusion profiles, similar results were obtained for YAG and pyrope annealed at 900 °C, suggesting limited effects of chemical composition on oxygen diffusivity. However, in both garnet types, a number of profiles deviate from the error function geometry, suggesting that the behavior of O in garnet cannot be fully described as simple concentration-independent diffusion, certainly in YAG and likely in natural pyrope as well. The experimental results are better described by invoking O diffusion via two distinct pathways with an inter-site reaction allowing O to move between these pathways. Modelling this process yields two diffusion

coefficients (*D*s) for O, one of which is approximately two orders of magnitude higher than the other. Taken together, Arrhenius relationships are:

$$\log D(\mathrm{m^2 s^{-1}}) = -7.2(\pm 1.3) + \left(\frac{-321(\pm 32)\mathrm{kJ mol^{-1}}}{2.303\mathrm{R}T}\right)$$

for the slow pathway, and

$$\log D(\mathrm{m^2 s^{-1}}) = -5.4(\pm 0.7) + \left(\frac{-312(\pm 20)\mathrm{kJ mol^{-1}}}{2.303\mathrm{R}T}\right)$$

for the fast pathway. We interpret the two pathways as representing diffusion following vacancy and interstitial mechanisms, respectively. Regardless, our new data seem to suggest that the slow mechanism is prevalent in garnet with natural compositions, thus is likely to control the retentivity of oxygen isotopic signatures in natural samples.

The diffusivity of oxygen is similar to Fe-Mn diffusivity in garnet at 1000-1100 °C and Ca diffusivity at 850 °C. However, the activation energy for O diffusion is larger, leading to lower diffusivities at *P-T* conditions characterizing crustal metamorphism. Therefore, original O isotopic signatures can be retained in garnets showing major element zoning partially re-equilibrated by diffusion, with the uncertainty caveat of extrapolating the experimental data to lower temperature conditions.

Keywords: oxygen isotopes; diffusion; piston cylinder experiments; gas mixing furnace; garnet; SIMS.

INTRODUCTION

Garnet is a key metamorphic mineral present in a variety of rocks and tectonic settings. It plays a crucial role in revealing thermal and mechanical processes controlling the evolution of Earth's crust at plate boundaries (Caddick and Kohn 2013) through its chemical and isotopic zoning. In particular, oxygen isotope heterogeneities in natural garnet crystals can record the infiltration of external fluids in metamorphic or hydrothermal systems, allowing for the determination of timing and rates of rock-fluid interactions in the crust (e.g., Kohn et al. 1993; Crowe et al. 2001; Skelton et al. 2002; Vielzeuf et al. 2005; Page et al. 2010, 2014; Sobolev et al. 2011; D'Errico et al. 2012; Errico et al. 2013; Russell et al. 2013; Martin et al. 2014; Rubatto and Angiboust 2015; He et al. 2019; Higashino et al. 2019; Gauthiez-Putallaz et al. 2020; Vho et al. 2020). Successful geothermobarometry and retrieval of accurate P-T-t-X_{fluids} paths relies on the assumption that mineral assemblages were formed at equilibrium. Equilibrium chemical and isotopic compositions can be modified by subsequent processes such as intra-crystalline diffusion or recrystallization, which can lead to erroneous inferred peak metamorphic P-T conditions (Eiler et al. 1993; Valley 2001; Chakraborty 2008; Ague and Carlson 2013; Baxter et al. 2013; Caddick and Kohn 2013).

The diffusivity of oxygen in garnet remains poorly constrained, even though it has been the focus of various studies in the past decades (Freer and Dennis 1982; Haneda et al. 1984; Coghlan 1990 unpublished data; Sakaguchi et al. 1996; Zheng and Fu 1998; Vielzeuf et al. 2005; Li et al. 2012). Only two experimental studies on garnet with geologically relevant compositions exist. Freer and Dennis (1982) were the first to investigate oxygen diffusivity in grossular garnet under wet conditions. However, no Arrhenius relation was determined because the experiments were done at different temperatures and pressures. The unpublished work of Coghlan (1990) investigated oxygen diffusivity in natural (almandine-spessartine) garnet, but reports a

discrepancy of ~2 log units between the diffusion coefficients calculated from his Arrhenius parameters and some of the raw data. We suspect this is simply due to a mislabeling of the *x*-axis in his Figure 2.1.a and assume that the quoted diffusivities and Arrhenius parameters are correct. Haneda et al. (1984) investigated oxygen diffusivity in yttrium aluminum garnet (YAG) by bulk analyses, which could conceivably be affected by fast diffusion paths or multiple diffusion mechanisms, whose influence might not be recognized without direct profiling (Zhang and Cherniak 2010). Because these previous experimental studies used different starting materials and experimental techniques/conditions, it is difficult to disentangle the potential effects of pressure, chemical composition, water and oxygen fugacity on oxygen diffusivity in garnet. This work aims to rectify this situation to some extent by experimentally constraining the effects of temperature, pressure and chemical composition on O diffusion in garnet.

EXPERIMENTAL PROCEDURE

Several experimental procedures were developed for this study, and experiments included variations of crystal chemistry, pressure, temperature and water activity. All experiments were performed at the Research School of Earth Sciences, Australian National University (ANU).

Starting material: crystals

Synthetic undoped YAG ($Y_3Al_5O_{12}$; Table S1, electronic supplement) was used for most experiments given its stability at high *T* (i.e., melting point ~1970 °C at 1 atm; Cockayne 1985) and low *P* (i.e., <1 atm), thus allowing investigation of oxygen diffusivity over a wide range of *P*-*T* conditions. Whilst the composition of YAG probably renders it geologically irrelevant for studying the behavior of cations in garnet, both YAG and pyrope have a cubic la3d crystal structure. Therefore, we make the first-order assumption that the oxygen sublattice of YAG is a

reasonable analogue for natural garnet, which is corroborated by analysis of the inter-oxygen spacing in YAG and pyralspite garnets (Fig. S1, electronic supplement). Nevertheless, natural crystals of grossular (Grs-2, ~$Grs_{94}Alm_4Adr_2$; provenance Afghanistan) and pyrope (Prp-1, ~$Prp_{70}Alm_{30}$; provenance Orissa, India), both purchased at mineral fairs, were also used to investigate the effect of chemical composition on oxygen diffusivity.

YAG was analyzed using a CAMECA SX-Five FE electron probe microanalyzer (EPMA) at the Department of Geoscience (University of Wisconsin-Madison, UW-Madison) (Table S1, electronic supplement). The composition of YAG starting materials and experimental run products was determined by collection of Y-Kα (LPET), Al-Kα (LTAP), and O-Kα (LPC0) X-rays at both 15 and 7 kV accelerating voltage, 20 nA beam current using a fully focused electron beam (~80 nm diameter; Moy and Fournelle 2017). Pyrope and grossular crystals were checked for chemical homogeneity with a JEOL JSM-6610A Scanning Electron Microscope (SEM) equipped with an energy-dispersive X-ray analysis (EDXA) system, at the Research School of Earth Sciences (ANU) (Table S2, electronic supplement). The three garnet starting materials contain less than 1.0 wt.% (2 standard deviation, 2SD) variation in major element composition.

Electron backscattered diffraction (EBSD) analysis was used to investigate the crystallographic orientation of the garnet in the near-interface region in some experimental charges. EBSD maps were collected at 20 kV, 20 nA using an Hitachi S3400 VP-SEM at the Department of Geoscience (UW-Madison) equipped with an Oxford EBSD detector.

Garnet cubes (~1 mm^3 and ~3 × 3 × 3 mm for piston-cylinder experiments, ~2 × 3 × 6 mm for 1-atm experiments) were cut using a 120 μm diamond-impregnated wafering blade on a low speed circular saw, and at least one face was polished with diamond paste to a 1 μm finish. Garnet cubes used for HP experiments were polished on their six faces to increase the number of

potential analytical surfaces after recovery. Polishing using a colloidal silica-based slurry was attempted once, but did not yield better-polished surfaces.

Starting material: powder sources

^{18}O-enriched diffusant source powders for nominally dry experiments at low- and high-pressure were prepared using the sol-gel method, which is superior to simply mixing together powders when working with refractory components. Firstly, Y_2O_3 powder and Al metal powder were weighed in proportions to give ~30 wt.% Al_2O_3 and 70 wt.% $Y_3Al_5O_{12}$. These were then dissolved, separately, in HNO_3 in Teflon ® beakers. The solutions were combined, left on a hot plate to reduce in volume, then a gel was precipitated by the addition of concentrated ammonia. The gel was dried, then the residue was placed into a Pt crucible and held over a Bunsen burner flame until visible fumes were no longer evolved. The crucible was then placed into a box furnace at 1200 °C to remove any remaining volatile components. Aliquots of the resulting powder were then placed into thick-walled, cold-sealed silver capsules (~6.3 mm outer diameter, OD) together with ^{18}O-enriched H_2O and annealed in an end-loaded piston-cylinder apparatus at T = 975 °C and P = 2.0 GPa for 48 h. This capsule design was described by Hack and Mavrogenes (2006) and is particularly suited for large-volume hydrothermal experiments because it can be cold-sealed by swaging in a hydraulic press. The fidelity of the experimental design, in terms of retaining water during experiments at equivalent *P-T-t* conditions, has been demonstrated previously (e.g. Jollands et al. 2016a; Tollan et al. 2018). After filling and swaging the capsules closed, each capsule was placed into an MgO-graphite-NaCl assembly (Fig. S2a). The temperature was monitored and controlled with a type B thermocouple ($Pt_{70}Rh_{30}$-$Pt_{94}Rh_6$) isolated by a two-bore mullite tube (or alumina-tipped mullite for T>1200 °C runs) and connected to a Eurotherm controller (Fig. S2a). A P of ~0.1 GPa was added before heating; then,

163 *T* was increased at 100 °C/min, and *P* was increased simultaneously with the aim of
164 approximately following an isochore, according to Hack and Mavrogenes (2006). The pressure
165 was manually adjusted throughout the experiment, as necessary. Experiments were quenched by
166 turning off the power – the temperature on the Eurotherm controller dropped to ~40 °C in a few
167 seconds (e.g., Hermann et al. 2016). The residual pressure was released gradually over ~30 min.
168 After the HP anneal, the YAG buffer was analyzed by X-ray diffraction in order to confirm
169 the synthesis of YAG plus corundum (Crn), the presence of which means that the yttria and
170 alumina activities are fully buffered (Warshaw and Roy 1959). The ^{18}O-enriched garnet buffer
171 was then ground to a fine powder under acetone in an agate mortar and used for gas mixing and
172 HP nominally dry experiments (see below). ^{18}O-enriched pyrope powder was prepared in a
173 similar way by annealing fine-grained pyrope (Prp-1) and ^{18}O-enriched H_2O in Ag capsules at *T*
174 = 900 °C and *P* = 1.0 GPa for 48 h.
175 Powders not enriched in ^{18}O were prepared simply by crushing pyrope and grossular to a fine
176 powder, or sintering a pellet of the Y_2O_3-Al_2O_3 mix prepared using the sol-gel method at 1400 °C
177 in air (i.e. instead of hydrothermal sintering with ^{18}O-enriched H_2O). These three powders were
178 used for HP experiments under water-present conditions (see below).
179
180 **Diffusion experiments and run products**
181 Major experimental challenges included: (1) ^{18}O exchange with the atmosphere in experiments
182 at atmospheric pressure, (2) the relatively low temperature stability of natural garnet, (3) the
183 effects of dissolution and precipitation in wet experiments and (4) the slow diffusivity of O,
184 which considerably limits the analytical possibilities. Therefore, several different setups and
185 experimental strategies were attempted (Table 1). From a total of 41 experiments only 16 were

186 successfully recovered and gave measurable ^{18}O profiles by SIMS (total of 68 diffusion profiles),
187 which yielded consistent results (Table 2).

188 **Gas mixing furnace experiments.** Experiments were conducted with YAG crystals, which
189 had been ultrasonically cleaned in ethanol, coated with ^{18}O-enriched YAG+Crn buffer powder
190 (see above) mixed with polyethylene oxide glue. The experimental charges (i.e., crystal+buffer)
191 were dried overnight in an oven at ~100 °C, placed into a platinum holder, and suspended inside
192 a gas mixing vertical tube furnace. Experiments were performed at 1500 °C and 1600 °C for 168
193 h and 24 h, respectively (Table 1). The final temperature was reached at a rate of 6 °C/min after
194 ramping up from 600 °C. The furnace was flushed with Ar to limit loss of ^{18}O from the buffer,
195 which means that the f_{O2} was not buffered, but instead controlled by impurities in the Ar gas. To
196 prevent crystals from breaking, experiments were ended by firstly cooling the furnace down to
197 ~600 °C at a rate of 5 °C/min and then pulling out the charges from the top of the furnace.

198 Crystals were recovered from 1-atm experiments at 1500 °C and 1600 °C. The ^{18}O buffer
199 sintered on the surface of the crystal and could not be removed by sonication (Fig. 1a). The
200 crystals were cut orthogonally to the diffusion interface, using a low-speed circular saw as above
201 (Fig. 1b). One of the halves of each crystal was mounted in epoxy, ground with SiC paper
202 (p1200, ~15 μm grit) and polished with diamond paste (3 μm and 1 μm) to be analyzed in line-
203 scan mode by SIMS (Figs. 1c-e). SEM imaging in cathodoluminescence (CL) mode shows a thin,
204 relatively dark CL band with constant thickness at the interface between the ^{18}O-YAG+Crn
205 buffer and the YAG cube (Fig. 1e; Table S3, electronic supplement) as well as along all other
206 edges of the crystal not in contact with the ^{18}O-buffer.

207 **High-pressure experiments under water-present conditions.** Experiments were conducted
208 using three different garnet compositions (i.e., YAG, Grs-2, and Prp-1). Garnet cubes (1 mm^3)
209 were embedded into a matrix made of a fine-grained powder of the same composition plus ^{18}O-

enriched H_2O (Fig. S3a, electronic supplement). A sintered YAG+Crn powder was used as the matrix for the YAG experiments (see above). Experiments with YAG, Prp-1, and Grs-2 were performed in end-loaded piston cylinder apparatus at T = 900 °C and P = 1.0 GPa for 14 days. A second experiment under these P-T conditions was conducted with a larger YAG cube (~3 × 3 × 3 mm) to enable preparation for backward depth-profiling analysis by SIMS. Additional experiments with YAG and Prp-1 were performed at T = 900 °C and P = 1.5 GPa for 14 days to investigate the effect of P on oxygen diffusivity (Table 1).

The experimental setup was similar to that used for the hydrothermal sintering of the source powders. For each experiment with YAG and pyrope, a layer of graphite powder was placed at the bottom of the silver capsule (Fig. S3a, electronic supplement) to buffer the f_{O2} (based on the buffered C-O-H equilibria; Connolly and Cesare 1993). For each experiment with grossular, the Re-ReO_2 oxygen buffer (Pownceby and O'Neill 1994) was used to produce more oxidizing conditions to stabilize the andradite component. A garnet cube was embedded into fine-grained garnet powder atop the f_{O2} buffer powder, then ^{18}O-enriched H_2O was added (Fig. S3a, electronic supplement).

Silver capsules recovered from the HP experiments under water-present conditions were pierced with a 1 mm drill bit to ensure water was still present and under pressure (i.e., no leaks formed during the experiment). The capsules were then opened on each face and crystals were removed, then cleaned ultrasonically to remove residual powder. The YAG crystals showed no evidence of dissolution, whereas the natural garnets did (Figs. 2a, b). In particular, grossular and pyrope crystals annealed at 1.0 and 1.5 GPa, respectively, were affected by intense dissolution that damaged the original diffusion interface and prevented further analysis. Pyrope annealed at 1.0 GPa (sample PHPW-1, Table 1) was affected by only localized dissolution (Fig. 2b), thus partially preserving the original diffusion interface. The best face of each recovered crystal was

mounted in epoxy for forward depth profiling analysis by SIMS (towards the crystal core; Tables 2 and S4, electronic supplement); these were not repolished. The recovered 3 × 3 × 3 mm YAG crystal was cut in half. One half was prepared and analyzed as above. The second half was ground to a thickness of ~10-12 μm and further polished to a final thickness of ~5 μm. It was then mounted in an epoxy disc for backward depth profiling analysis by SHRIMP (towards the crystal rim; low to high ^{18}O with increasing depth) to estimate the extent of edge effects (i.e., the contribution to the diffusion profile arising from secondary ions sputtered from the edge of the crater) with this instrument.

High-pressure experiments under nominally anhydrous conditions. This experimental approach was developed to overcome some of the difficulties encountered during the hydrous experiments, mainly dissolution occurring in the presence of water and relatively low melting temperatures of the silver capsule material. Diffusion under nominally anhydrous conditions was thus investigated using garnet cubes embedded into a matrix made of graphite powder and fine-grained powder of YAG+Crn previously enriched in ^{18}O (see above; Figs. S3b, c, electronic supplement). Graphite was added with the aim of limiting sintering of the garnet powder onto the cube, as in Van Orman et al. (2001, 2002). The proportions of graphite to garnet powder were always kept constant (i.e., 2:1 ratio by weight). No water was added to these runs.

Experiments with YAG were conducted over the T range of 1050-1600 °C at P = 1.5 GPa. An additional experiment with YAG was conducted at T = 1500 °C and P = 2.5 GPa to further investigate the effect of pressure on oxygen diffusivity (Table 1). An experiment with pyrope (Prp-1) was also attempted at T = 1200 °C and P = 1.5 GPa for 48 h. Experiments were conducted either in platinum capsules (3.5 mm OD) or graphite-lined platinum capsules (5 mm OD) to limit garnet-platinum interaction, most notably Fe loss to the capsule (Figs. S3b, c, electronic supplement). The lined capsule technique was first tested on YAG annealed at T =

1200 °C and 1600 °C, P = 1.5 GPa (YHPD-1 and YHPD-10, Table 1). The capsules were filled with the graphite+^{18}O-enriched garnet powder surrounding a garnet cube (Figs. S3b, c, electronic supplement). Most experiments were conducted with the piston cylinder assembly described above, a modification being the addition of borosilicate glass between the graphite heater and NaCl at T>1000 °C and P = 1.5 GPa (Akella et al. 1969), and an MgO shield above the capsule (Fig. S2b).

Most of the recovered capsules were mounted in epoxy and polished for line-scan analysis by SIMS (Figs. 2c-f). Three other capsules were opened, and crystals removed and cleaned, as above, and mounted in epoxy for forward depth profiling. All recovered YAG crystals were in good condition, with the exception of some fractures (e.g., Fig. 2d) that probably developed during decompression upon quenching.

PREPARATION AND IMAGING OF SIMS MOUNTS

All experimental charges were mounted, together with the corresponding garnet reference material, in the central part of 25.4 mm epoxy discs. The integrity of the diffusion interface was checked either by a Leica DM6000_M automated microscope in reflected light mode or by SEM imaging in Backscattered Electron (BSE) and CL modes (Figs. 1, 2, 3). Prior to analysis by SHRIMP, mounts were coated with 15 nm of aluminum or gold after chemical cleaning. Prior to analysis with a CAMECA IMS-1280, mounts were coated with ~60 nm thick gold. Samples were kept in a vacuum oven at 60 °C for at least 48 h before being introduced into the instruments.

For NanoSIMS analyses, crystals were removed from their epoxy mounts and pressed into indium (preferable to epoxy for maintaining ultra-high vacuum ~10^{-8} Pa) in 25 mm aluminum holders, which were then gold-coated (15 nm).

SHRIMP traverses were imaged with a LEICA DM6000_M automated microscope (Research School of Earth Sciences, ANU) that allowed the average distance of each spot perpendicular from the diffusion interface to be measured. Traverses measured by NanoSIMS were imaged with a JSM-6610A SEM at the Research School of Earth Sciences (ANU) in BSE and Secondary Electron (SE) mode. Traverses measured with a CAMECA IMS-1280 were imaged using an Hitachi S3400 SEM at the Department of Geoscience (UW-Madison) using BSE and SE imaging modes. In addition, traverses in three experimental charges were also imaged in CL mode using a Gatan Pana/CL/F system. Finally, SHRIMP and CAMECA IMS-1280 pits from depth profiling analyses were imaged with a Leica DCM8 confocal microscope (Research School of Earth Sciences, ANU) and a ZYGO white-light interferometer (Department of Materials Science and Engineering, UW-Madison), respectively, to check their geometry and to measure their depth.

ANALYTICAL METHODS FOR OXYGEN ISOTOPE ANALYSIS

In this study, oxygen diffusion profiles were measured using SHRIMP, CAMECA IMS-1280 and NanoSIMS N50L instruments, in line-scan or depth profiling mode. Garnet crystals not annealed under experimental conditions and having a comparable chemical composition to the experimental charges (hereafter referred to as garnet reference materials) were analyzed simultaneously with the experimental charges to monitor potential analytical artifacts during depth profiling that could affect the shape of diffusion profiles measured in the experimental charges. A detailed explanation of the different analytical setups used in this study is given in Electronic Appendix 1.

DATA TREATMENT AND FITTING OF PROFILES

The standard practice in such studies as this is to fit the measured profiles to a concentration-independent, constant boundary condition, one-dimensional, semi-infinite media solution to Fick's second law:

$$\frac{C(x,t)-C_0}{C_1-C_0} = 1 - \mathrm{erf}\,\frac{x}{2\sqrt{Dt}} \quad (1)$$

where $C(x,t)$ is the concentration (C) at the distance x (m), from the interface, and time t (s); C_1 is the concentration at the interface (or surface concentration); C_0 is the initial concentration in the mineral (or background concentration); D is the diffusion coefficient (m^2s^{-1}). For this to be valid, profiles should all correspond to the form of an error function, which requires concentration-independent diffusion. Whilst a minority of $^{18}O/(^{18}O+^{16}O)$ profiles do have such geometry (Fig. 4) and could be fitted using Equation 1, the majority of profiles acquired in this study do not. In the latter case, the tail ends of the profiles were extracted and fitted to Equation 1. This gives an approximate diffusion coefficient (we denote this $\widetilde{D}$) equivalent to that which would be obtained using the $x = 4\sqrt{(Dt)}$ approximation by visual estimation of the profile lengths. For profiles with complex shapes that cannot be fitted to Equation 1, these $\widetilde{D}$s are useful as a first-order estimate only. A model for extracting meaningful/useful diffusion coefficients (Ds) from profiles of complex shapes is discussed below. We note that, in this study, the fraction of ^{18}O (i.e., $^{18}O/(^{18}O+^{16}O)$) is considered to be the equivalent of the absolute concentration.

RESULTS

Profile shapes

Broadly, three different $^{18}O/(^{18}O+^{16}O)$ profile geometries were encountered during this study.

1) 'Stepped' profile shapes, which refers to profiles with two or three distinct sections/zones from the outside to the inside of the crystal (Fig. 5; Table S5, electronic supplement), as

described below. Zone I is characterized by a relatively steep decrease in the $^{18}O/(^{18}O+^{16}O)$ ratios. This zone is observed in the YAG cubes annealed at T = 1400 °C and P = 1.5 GPa for 95.5 h (Fig. 5a) and 2 h (Fig. 5b). It is also hinted at the YAG cube annealed at T = 1200 °C and P = 1.5 GPa for 24 h (Table S5, electronic supplement). Zone II is characterized by a shallower slope than zone I and by a quasi-linear decrease in the $^{18}O/(^{18}O+^{16}O)$ ratios with increasing distance from the interface (Figs. 5a-c). This zone is observed in all samples with complexly shaped profiles. In crystals where also zone I is observed, zone II is identified by a change in the slope of the curve (Figs. 5a-b). Zone III is identified by another change in the slope of the curve where the $^{18}O/(^{18}O+^{16}O)$ ratios decrease more rapidly than zone II until they reach the initial oxygen isotope composition (Figs. 5a-e). This region is observed in all samples. Such stepped profiles are encountered in all HP nominally dry experiments, with the exception of the one annealed at T = 1050 °C (sample YHPD-1; Table S5, electronic supplement).

2) Certain profiles correspond to an error function form, i.e., described by Equation 1. These are encountered in the low-P and high-T runs (samples YLPD-1 and YLPD-2; Table S3, electronic supplement), as well as the HP and low-T hydrothermal runs (Table S4, electronic supplement). In the latter, however, the shape of the diffusion profiles is dependent on the chosen position of the interface (see Electronic Appendix 2).

3) Profiles with a broadly error function form, but that have an excessively long tail towards background values. These include only a CAMECA IMS-1280 profile (i.e., profile 1 in sample PHPW-1 annealed at 1.0 GPa and 900 °C; Table S4, electronic supplement).

Gas mixing furnace experiments

The measured concentration-distance profiles in two YAG cubes annealed in the gas mixing furnace at T = 1600 °C for 24 h and 1500 °C for 168 h (Tables 1, 2 and S3, electronic

supplement) follow an error-function shaped curve (Fig. 4), which could be fitted using Equation 1. Comparable estimated diffusion coefficients (D) were calculated from profiles measured with SHRIMP ($\log D$ = –14.4±0.2 m^2s^{-1} at 1600 °C and –14.8±0.2 m^2s^{-1} at 1500 °C) and CAMECA IMS-1280 ($\log D$ = –14.7±0.1 m^2s^{-1} at 1600 °C and –15.1±0.2 m^2s^{-1} at 1500 °C) (Fig. 4; Table 2).

High-pressure experiments under water-present conditions

Recrystallization of the surrounding matrix on top of the original crystal is observed in the four experiments (Table 1). During forward depth profiling, $^{18}O/(^{18}O+^{16}O)$ ratios increase progressively (towards the center of the cube) in the overgrowth and drop dramatically when crossing the interface between overgrowth and garnet cube (Table S4, electronic supplement). The drastic drop in OH/O signal in profiles measured by CAMECA IMS-1280 (Table S4, electronic supplement) allowed us to objectively locate the interface between nominally dry YAG cubes and overgrowths formed during wet experiments (see Electronic Appendix 2 for details). Profiles measured in forward and backward profiling mode by CAMECA IMS-1280 have similar lengths and shapes confirming the limited extent of edge effects with IMS-1280 instruments (Table S4, electronic supplement). On the contrary, forward profiles measured by SHRIMP have longer tails when compared to backward profiles suggesting the occurrence of significant edge effects (Table S4, electronic supplement). Additionally, CAMECA IMS-1280 profiles are overall shorter compared to those measured by SHRIMP (including the backward profiles) resulting in approximate $\log\widetilde{D}$s slower by ~1-2 log units (Table 2). Consequently, only data acquired with a CAMECA IMS-1280 in these experimental charges are further discussed.

In contrast to the low-pressure experiments, the shape of the concentration-distance profiles for YAG annealed at HP in water-saturated conditions is not consistent with error function forms

374 (Table S4, electronic supplement), thus Equation 1 is inappropriate. The formation of such
375 profiles will be discussed below.
376 Similar approximate diffusivities were determined for YAG annealed at 900 °C and different
377 pressures ($\log\widetilde{D}$ = –21.3±0.9 m^2s^{-1} at 1.0 GPa, combining all data from samples YHPW-1 and
378 YHPW-2, and –21.6±0.3 m^2s^{-1} at 1.5 GPa) (Table 2). Profiles across pyrope annealed in similar
379 experimental conditions as YAG (T = 900 °C, P = 1.0 GPa) return data that are consistent with an
380 error function curve (with the exception of profile 1 that was excluded from calculations of
381 diffusion coefficients; Table S4, electronic supplement). From the fit, the calculated diffusion
382 coefficient ($\log D$ = –21.2±0.7 m^2s^{-1}) is within uncertainty identical to that obtained from
383 experiments with YAG (Table 2).
384
385 **High-pressure experiments under nominally anhydrous conditions**
386 Ten YAG cubes annealed at P = 1.5-2.5 GPa and T = 1050-1600 °C under nominally
387 anhydrous conditions were analyzed (Tables 2 and S5, electronic supplement). All samples
388 except the one annealed at 1050 °C have 'stepped' concentration-distance profiles (Fig. 5; Table
389 S5, electronic supplement). EPMA transects show no obvious variation in Y, Al, or O across the
390 width of the YAG crystal or within the diffusion-affected region (Electronic Appendix 3). EBSD
391 analysis indicates that YAG substrate, diffusion-modified rim, and buffer-quench overgrowth are
392 a crystallographically continuous single crystal of YAG (Electronic Appendix 3).
393 Approximate average $\log\widetilde{D}$s for experimental charges annealed under nominally dry
394 conditions at HP are summarized in Table 2. Notably, oxygen diffusivity calculated from profiles
395 measured in depth profiling mode are comparable within uncertainty to those estimated from
396 NanoSIMS traverses (Table 2).

First-order approximation of the Arrhenius relationship

Diffusivities calculated from fitting either the tail-ends of profiles ($\widetilde{D}$), or the whole profile to Equation 1, where appropriate (D), result in the following first-order Arrhenius relationship (Fig. 6):

$$\log\widetilde{D}(\mathrm{m^2s^{-1}}) = -3.8(\pm0.7) + \left(\frac{-394(\pm19)\mathrm{kJmol^{-1}}}{2.303\mathrm{R}T}\right) \quad (2)$$

where R is the gas constant ($\mathrm{kJK^{-1}mol^{-1}}$), T is the temperature (K) and uncertainties represent 95% confidence bounds (±2σ). Notably, if only data calculated from error-function shaped profiles (i.e., samples YLPD-1, YLPD-2, YHPD-1 and PHPW-1; Table 2) are fitted to Equation 1, Arrhenius parameters are within uncertainty of those reported above considering the full dataset.

In this study, oxygen diffusion coefficients in garnet annealed at various P and constant T (i.e., 1600 °C, 1500 °C, and 900 °C) show contrasting trends (negative D-P correlation at 1600 °C and 900 °C, no correlation at 1500 °C) (Fig. S4, electronic supplement). This, along with the large uncertainty on the first order approximate diffusion coefficients, prevents the effect of P on oxygen diffusivity in garnet under either nominally dry or water-saturated conditions to be determined; small discrepancies between the data might be due to differences in f_{O2}, or f_{H2O} between low- and high-P experiments.

The results obtained in one pyrope annealed in similar P-T conditions as YAG suggest no significant effect of chemical composition within the uncertainties of the data (Fig. 6, Table 2). Finally, it was not possible to investigate the effects of water (i.e. f_{H2O}) on oxygen diffusivity at T>900 °C. Nevertheless, log$\widetilde{D}$s calculated for water-saturated experiments at 900 °C fall on the Arrhenius curve described by nominally dry experiments (Fig. 6) and future experimental studies

should verify whether a similar slope can be expected for oxygen diffusivity in garnet under wet conditions and quantify the effects of water (and f_{H2O}).

DISCUSSION

Diffusion mechanism and diffusion coefficient determination

As described above, the majority of acquired profiles of $^{18}O/(^{18}O+^{16}O)$ versus distance from the crystal edge do not conform to any analytical solutions of Fick's second law for reasonable initial and boundary conditions. This suggests that the assumption that the profiles can be described simply as resulting from a single diffusion mechanism is not valid.

It could be suggested that stepped profiles are the result of the overgrowth of a garnet rim followed by diffusive exchange between the new rim and original crystal. Whilst this may be valid for the HP wet experiments, there is no justification for invoking overgrowth in a nominally dry experiment where the crystal and O-source powder are nominally in major element equilibrium, and where the polished crystal faces were generally recovered after the experiments. These stepped profiles are similar to those reported by Dohmen et al. (2010) for Li diffusion in olivine, and by Jollands et al. (2016b) for Ti diffusion in olivine. Dohmen et al. (2010) described their profile shapes by assuming that Li occupied two distinct positions (interstitial or lattice sites) in olivine, and that each of these positions was associated with a different diffusion mechanism and hence diffusivity. Allowing Li to exchange between these positions enables the creation of profiles with stepped shapes. The formation of such profiles can be broadly described as resulting from a species diffusing rapidly along one pathway, then hopping into another site (which has some finite capacity to accommodate the diffusing species), after which the species becomes relatively immobile. The stepped profiles then represent a wave of the diffusing species moving into the crystal rapidly along one pathway, then moving into, and filling up, the available

444 sites in the other pathway. The model presented herein follows similar logic based on
445 considerations of O-substitution and diffusion in olivine (e.g., Gérard and Jaoul 1989; Ryerson et
446 al. 1989; Costa and Chakraborty 2008). The main point is that the behavior of O in garnet cannot
447 be fully described as simple concentration-independent diffusion on a single crystallographic site,
448 certainly in YAG and likely in natural pyrope as well.

449 **Diffusion model.** First principle calculations of intrinsic point defects in YAG have shown
450 that there are two main oxygen defect types: oxygen vacancies ($V_O^{\bullet\bullet}$) and interstitial oxygen O_i''
451 (Li et al. 2012). Based on this, it is suggested that the two diffusion pathways for O could involve
452 (1) O^{2-} on its own lattice site, i.e. in Kröger-Vink notation, $O_O^{\times}$ diffusing by a vacancy
453 mechanism; and (2) O on an interstitial site, O_i''. It is implicitly assumed that interstitial O^{2-} is
454 charge balanced. O_i'' is arbitrarily designated as more mobile, i.e. $O_O^{\times}$ has lower diffusivity than
455 O_i''. Finally, there must be some available site into which the more mobile O_i'' can relocate, which
456 reduces its mobility. For this, vacant O sites are invoked, i.e. $V_O^{\bullet\bullet}$.

457 With these assumptions, a simple exchange reaction is written, wherein O_i'' moves into a
458 vacant oxygen site, forming $O_O^{\times}$, i.e. the reaction describing an O Frenkel defect:

459 $$O_i'' + V_O^{\bullet\bullet} = O_O^{\times} \quad (3)$$

460 Another simplification of the model is that ^{18}O is treated as a trace element, i.e., ^{16}O is
461 explicitly not considered. A discussion of the implications of the omission of ^{16}O is provided in
462 Appendix 2. Consequently, Equation 3 can be written in terms of ^{18}O as:

463 $$^{18}O_i'' + V_O^{\bullet\bullet} = {}^{18}O_O^{\times} \quad (4)$$

464 From Equation 4, an equilibrium expression is constructed:

465 $$K = \frac{[{}^{18}O_O^{\times}]}{[{}^{18}O_i''][V_O^{\bullet\bullet}]} \quad (5)$$

where brackets represent concentrations per 12 oxygens. To describe uniquely the concentrations of $^{18}O_i''$, $V_O^{\bullet\bullet}$ and $^{18}O_O^{\times}$, two other variables need to be fixed. These are the sum of ^{18}O:

$$\sum^{18}O = [^{18}O_i''] + [^{18}O_O^{\times}] \quad (6)$$

and the total number of O sites in the YAG lattice (i.e. excluding the interstitial sites) occupied by either $^{18}O_i''$ or $V_O^{\bullet\bullet}$:

$$\sum X_O = [V_O^{\bullet\bullet}] + [^{18}O_O^{\times}] \quad (7)$$

If K, $\sum^{18}O$ and $\sum X_O$ are defined, then the concentrations of $^{18}O_i''$, $V_O^{\bullet\bullet}$ and $^{18}O_O^{\times}$ are calculated by solving Equations A2.1 to A2.3 (Electronic Appendix 2).

With these equations, the system can be modelled using a two-step explicit finite difference routine, wherein the total time of the diffusion experiment is divided into many time steps, with the number of steps variable, but defined by the resolution of the model and the highest diffusion coefficient to retain numerical stability. In the first part of each time step, diffusion occurs. Concentration-independent diffusion is assumed. Diffusion was modelled separately for each of the three species of interest ($^{18}O_i''$, $V_O^{\bullet\bullet}$ and $^{18}O_O^{\times}$), using three diffusion coefficients. In the second step, the inter-site reaction occurs according to Equation 3. Then, the next time step begins with diffusion, then reaction, and so on, until the total experimental time is reached. The inputs of the model are K, three Ds, and the interface and initial values of $\sum^{18}O$ and $\sum X_O$. The output of the model is the concentration of each species as a function of distance after a model time corresponding to the duration of the experiment. The model is then fitted to the data with some fit parameters presented in Table 2. A full description of the routine is presented in Appendix 2, but a brief description is as follows. Firstly, $\sum^{18}O$ at the interface was set manually based on visual inspection of the profiles, and $\log_{10}$K was set at some value, normally between 0 and 4. Then, the best fit values of $\sum X_O$ (interface and initial), $\sum^{18}O$ (background) and the three

489 *D*s were determined by nonlinear least squares regression. This was then repeated for many
490 values of $\log_{10}$K, and the fit parameters associated with the lowest summed square of residuals
491 were taken to be the parameters defining the best fit. Examples fits of profiles measured in HP
492 experiments are shown in Figure 7. Uncertainties on the fit parameters are not presented in Table
493 2, but we estimate that 2s uncertainty on $\log_{10} D^{18}O_O^{\times}$ is 0.03 to 1 m^2s^{-1} and 0.01-0.05 m^2s^{-1} on
494 $\log_{10} D^{18}O_i''$. Further information is provided in Appendix 2.

495 Whilst we model the profiles using the relationship in Equation 4, we emphasise that this is
496 only one possible model. Any situation including 1) a substitution mechanism associated with
497 low concentration and fast diffusion; 2) a slow diffusion, high-concentration substitution
498 mechanism and 3) a reaction allowing exchange between these two sites, could potentially
499 produce profiles with such stepped shapes as observed here. For example, given that the stepped
500 shapes are only observed following piston cylinder experiments, and even the 'dry' experiments
501 will be only nominally dry (cf. absolutely dry), one could invoke a reaction such as:

502 $$^{18}OH_i' + V_O^{\bullet\bullet} = {}^{18}O_O^{\times} + H_i^{\bullet} \quad (8)$$

503 Likewise, a mechanism could be invoked involving interstitial O charge-compensated by
504 interstitial Al^{3+}, or some other cation:

505 $$\{^{18}O_i'' - Al_i^{\bullet\bullet\bullet}\}^{\bullet} + V_O^{\bullet\bullet} = {}^{18}O_O^{\times} + Al_i^{\bullet\bullet\bullet} \quad (9)$$

506 Or, some strain-induced extended defect that enables fast diffusion could be invoked.
507 However, if we can assume that it is the slow mechanism that is relevant for O diffusion in
508 natural garnet (discussed below), then the specific definition of the fast mechanism is relatively
509 unimportant. Based on our EBSD, EPMA and X-ray map investigations as well as the
510 consistency between profiles we can, however, rule out surface recrystallization as an explanation
511 for the profile shapes.

Arrhenius relations. The results from the profiles that were fitted to Equation 1 (where appropriate) and to the reaction-diffusion model are shown in Figure 8. Effectively, most profiles that required the diffusion-reaction model show that the two O diffusion coefficients (which we designate $D^{18}O_O^{\times}$ and $D^{18}O_i''$) are different by approximately two orders of magnitude (Table 2). This is the case over the full range of temperature studied, and for both pyrope and YAG, suggesting that the two diffusion mechanisms have similar activation energies. Profiles from the 900 °C experiments that were fitted using an error function shape (Equation 1) yield diffusion coefficients in agreement with the slow mechanism, and profiles from the 1500 and 1600 °C experiments fitted using the same equation yield *D*s that agree with those associated with the faster mechanism. The profile from the 1050 °C experiment that was fitted using Equation 1 yielded *D*s in agreement with the fast mechanism.

Therefore, taking all of the *D*s associated with the fast mechanism from diffusion-reaction modelling, as well as the data from the 1050 °C experiment fitted to Equation 1, a general Arrhenius relationship can be defined:

$$\log D(\mathrm{m^2 s^{-1}}) = -5.4(\pm 0.7) + \left(\frac{-312(\pm 20)\mathrm{kJmol^{-1}}}{2.303\mathrm{R}T}\right) \quad (10)$$

where uncertainties represent 95% confidence bounds (±2σ). Likewise, taking all of the *D*s associated with the slow mechanism, plus those extracted using Equation 1 for the low temperature runs, and the data of Coghlan (1990 unpublished data) that fall on our calibration, we obtain:

$$\log D(\mathrm{m^2 s^{-1}}) = -7.2(\pm 1.3) + \left(\frac{-321(\pm 32)\mathrm{kJmol^{-1}}}{2.303\mathrm{R}T}\right) \quad (11)$$

533 Both of these fits are unweighted; given the issues described above regarding the low sensitivity
534 of the residuals of each fit on the values of some $D^{18}O_O^{\times}$, determining any meaningful
535 uncertainties using our fitting routine is precluded. The data from the 1500 °C and 1600 °C
536 experiments that were fitted to error function curves (Equation 1) are not included in either fit
537 because it is not clear whether the associated *D*s should be assigned to the fast or slow
538 mechanism.
539 Note that these relationships do not include any garnet composition, f_{H2O} nor pressure term, as
540 we find no systematic effect of these variables on diffusion. That the values obtained from YAG
541 (slow mechanism) and pyrope (this study) and almandine-spessartine (Coghlan, 1990
542 unpublished data) are in agreement suggests that any compositional effect on O diffusion is
543 minor – this is extremely promising when considering the applicability of data derived from
544 experiments with unnatural endmember compositions that can withstand a broader range of *P*-*T*-
545 *X* conditions (i.e. YAG) than their natural counterparts.
546 **Variations in profile shapes.** One first-order observation is that there is some inconsistency
547 concerning profile shapes from different experiments. For example, many of the 1-atm
548 experiments at 1500 °C and 1600 °C show profiles with error function forms, whereas all of the
549 HP 1200-1400 °C experiments show stepped shapes. Then, the HP experiment at 1050 °C shows
550 an error function form with *D*s consistent with the fast mechanism, whereas the HP experiments
551 at 900 °C, when fitted to an error function, show *D*s consistent with the slow mechanism. The
552 same can be said for the Coghlan (1990 unpublished data) data – regardless of the relatively poor
553 spatial resolution of his profiles, they seem to show error function forms consistent with our slow
554 diffusivities. We cannot explain conclusively why this is the case, but offer some suggestions.
555 Figure 9a shows a diffusion reaction model wherein all parameters, except the interface ^{18}O
556 concentration, are kept constant. As the interface concentration decreases, the profiles tend

557 towards an error function shape, and become shorter. Alternatively, Figure 9b shows the results
558 of a model where all parameters except *K* are kept constant. As *K* increases, the profile again
559 tends towards an error function, but here the length approaches that associated with the fast
560 mechanism. Similarly, the shape can be changed by modifying the concentration of defects in the
561 starting material – this would be unreasonable considering that the experiments were done with
562 the same starting material, but might go some way towards explaining differences between the
563 YAG and natural garnet profiles.
564
565 **Comparison with previous studies**
566 Oxygen diffusion in garnet has previously been investigated by several authors (Freer and
567 Dennis 1982; Haneda et al. 1984; Coghlan 1990 unpublished data; Sakaguchi et al. 1996; Zheng
568 and Fu 1998; Vielzeuf et al. 2005; Li et al. 2012) using different methodologies (e.g.,
569 experiments, calibrations in natural samples, first-principle investigations). No studies report
570 profiles with complex shapes such as those that we observe, but all results fall within the range of
571 the two Arrhenius relationships that we have identified.
572 Freer and Dennis (1982) reacted natural crystals of grossular with water enriched in ^{18}O at T =
573 850 °C (P = 0.2 GPa) and T = 1050 °C (P = 0.8 GPa), and measured diffusion profiles by SIMS
574 depth profiling. They obtained diffusivity values that agree with our fast diffusion mechanism at
575 850 °C (log$D$ = –20.3 m^2s^{-1}) and slow diffusion mechanism at 1050 °C (log$D$ = –19.6 m^2s^{-1}) (Fig.
576 10a), and it is not clear why this is the case. Coghlan (1990 unpublished data) performed
577 experiments at constant water pressure (0.1 GPa) and temperatures between 800 °C and 1000 °C
578 by hydrothermal exchange between ^{18}O-enriched H_2O and natural almandine-spessartine garnet
579 crystals (~$Alm_{70}Sps_{30}$), suggesting diffusivity values up to ~2 log units slower than that obtained
580 by Freer and Dennis (1982) at 850 °C (Fig. 10a). The Coghlan (1990 unpublished data) data

581 agree well with our slow mechanism, so we propose that our study and the Coghlan (1990
582 unpublished data) study were measuring the same process. The assumptions of the diffusion-
583 reaction model suggest that this process represents O diffusion on the O site.
584 Haneda et al. (1984) investigated oxygen diffusivity in YAG by the gas-solid isotope
585 exchange technique (P = 1 atm) using oxygen gas enriched with about 20% ^{18}O as a tracer at
586 temperatures of 1060 °C to 1550 °C. The authors observed a variation in D_0, depending on the
587 composition of the atmosphere in which YAG crystals were pre-heated before diffusion
588 annealing (i.e., air, $D_0 = 2.34 \times 10^{-8}$ m^2s^{-1}; aluminum vapor, $D_0 = 8.13 \times 10^{-7}$ m^2s^{-1}; nitrogen, $D_0 =$
589 5.24×10^{-7} m^2s^{-1} similar to YAG that was not pre-heated). The composition of the atmosphere in
590 the pre-heating stage affects the oxygen vacancy levels. The Arrhenius relations proposed by
591 Haneda et al. (1984) for YAG pre-heated in air (their 'O-YAG') and aluminum vapor ('FC-YAG')
592 are in good agreement with our slow and fast diffusion mechanisms, respectively, whereas the
593 Arrhenius relation for YAG not pre-heated ('AG-YAG') or pre-heated in nitrogen atmosphere
594 ('N-YAG') falls in between our two calibrations (Fig. 10a). First principle calculations of intrinsic
595 point defects in YAG (Li et al. 2012) show that the formation of Al_Y anti-site defects (i.e., the
596 substitution of Y with Al in a lattice site) lowers the energy barrier for O diffusion, and explain
597 the faster O diffusivity observed if an excess of Al is available. Thus the buffering with
598 corundum in our experiments might have led to a similar fast pathway. Nevertheless, it is not
599 straightforward to compare our results with those of Haneda et al. (1984) because the latter did
600 not buffer the Al_2O_3.
601 Sakaguchi et al. (1996) studied the effect of chemical composition on oxygen volume and
602 grain-boundary diffusion in different YAG ceramics (i.e., 2% and 1% excess Y_2O_3,
603 stoichiometric, and 0.5% excess Al_2O_3). All samples were reacted with $^{18}O_2$ at ~17 kPa in the T
604 range 1100 °C to 1385 °C and diffusion profiles were measured by SIMS. The authors observed

605 that volume diffusion of oxygen is little influenced by the excess composition, whereas grain
606 boundary diffusion is suppressed in the Y_2O_3-excess samples and enhanced in the Al_2O_3-excess
607 ones. Our calibration for the slow diffusion mechanism agrees well also with the Arrhenius
608 relationship proposed by Sakaguchi et al. (1996) for volume diffusion in stoichiometric YAG not
609 annealed before the experiments (Fig. 10a).
610
611 **Oxygen versus cation diffusion in garnet**
612 Several authors have determined the diffusivities of major (e.g., Fe, Mg, Ca, and Mn) and
613 minor cations (e.g., REEs) in garnet (e.g. Ganguly 2010 for a review). Unlike oxygen, diffusion
614 of major cations in garnet has to be treated as part of a multicomponent system in which the
615 diffusivities of each component have to be constrained (Lasaga 1979). According to our study,
616 oxygen diffuses at a rate that is comparable to those observed for the fastest major cations in
617 garnet at higher temperatures (Fig. 10b). In particular, the slow oxygen diffusion mechanism is
618 comparable to self-diffusivities calculated for Mn and Fe in the pyrope-almandine diffusion
619 couple by Ganguly et al. (1998). However, unlike for oxygen, the diffusivity of cations in garnet
620 is significantly affected by chemical composition (e.g., Chakraborty and Ganguly 1992; Ganguly
621 et al. 1998; Borinski et al. 2012).
622 Vielzeuf et al. (2005) measured compositional profiles of major cations (Mg, Mn, Fe, Ca) at
623 the core-rim interface of zoned garnet crystals. The profiles are consistent with a relaxation of an
624 initial sharp step in Ca, Mg, and Fe by Ca ↔ (Fe, Mg) interdiffusion. At the same interface, the
625 authors observed an oxygen isotope profile comparable to that described by Ca and suggest that
626 Ca and oxygen have similar relative diffusivities on the order of $\log D$ (m^2s^{-1}) = – 21.9, as
627 calculated by Vielzeuf et al. (2007) for Ca. Extrapolation of our slow calibration to T = 850 °C
628 results in a $\log D$ (m^2s^{-1}) of – 22.2±0.4 (2σ) for oxygen that is comparable within uncertainty to

629 the diffusivity of Ca (Vielzeuf et al. 2007). The fast calibration was not extrapolated to lower *T*s
630 because the fast mechanism is less applicable to natural garnets.
631 Despite comparable diffusivities between oxygen and divalent cations, the activation energy
632 for oxygen diffusion is higher than that of major divalent cations, suggesting that the
633 extrapolation of experimental results to temperatures typical of crustal conditions (T<850 °C)
634 would result in slower oxygen diffusivity relative to major cations (Fig. 10b).
635
636 **Diffusion chronometry**
637 Oxygen isotopic heterogeneities in garnet at the microscale have been observed in various
638 geological settings by several workers, but only a few studies have reported profiles that were
639 attributed to diffusion (e.g., Vielzeuf et al. 2005; Page et al. 2010; Higashino et al. 2019). Herein,
640 we discuss the results of re-fitting some published data with our new, slow Arrhenius relationship
641 (Fig. 11).
642 Page et al. (2010) measured a <50 μm long profile with a 2.1‰ $\delta^{18}O$ change in a skarn garnet
643 that underwent regional granulite-facies metamorphism at peak temperature of 750 °C. Following
644 the original interpretation, diffusion is modelled by assuming an initial step function, with the
645 step located at x=X, and the initial concentrations on either side of the step being C_1 and C_0.
646 Diffusion is then modelled assuming plane sheet geometry, which is reasonable given that the
647 length scale of the diffusion profile is much lower than the size of the crystal:

648 $$C(x,t) = C_0 + \tfrac{1}{2}(C_1 - C_0)\mathrm{erfc}\left(\frac{x-X}{2\sqrt{Dt}}\right) \quad (12)$$

649 (Crank 1975). Fitting their data gives a best fit logDt (m^2) of –10.8, an upper limit (+2σ) of –10.5,
650 whereas the lower limit of Dt is 0. Taking just the upper bound of logDt, and the lower limit

651 (mean minus 2σ) of log$D$ (m^2s^{-1}) at 750 °C (i.e., –24.2), the maximum time for diffusion is 1.6
652 M.y..

653 Higashino et al. (2019) reported $\delta^{18}O$ profiles across a core-rim transect in almandine-pyrope
654 garnet. The length scale over which $\delta^{18}O$ changed is >500 μm in a garnet with a rim-to-rim
655 distance of ~3.5 mm, thus plane sheet geometry is inappropriate. Therefore, a spherical geometry
656 for garnet is used with radius R and composition C_0 (i.e. the core), surrounded by a large volume
657 of garnet with composition C_1 (i.e. the overgrowth). For this geometry, the concentration at radial
658 distance r (given as distance from the crystal core) is:

659 $$C(r,t)=C_1+\frac{1}{2}(C_0-C_1)\left(\mathrm{erf}\left(\frac{R+r}{2\sqrt{Dt}}\right)+\mathrm{erf}\left(\frac{R-r}{2\sqrt{Dt}}\right)\right)-$$

660 $$-\frac{(C_0-C_1)}{r}\sqrt{\left(\frac{Dt}{\pi}\right)}\left(\exp\left(-\frac{(R-r)^2}{4Dt}\right)-\exp\left(-\frac{(R+r)^2}{4Dt}\right)\right) \quad (13)$$

661 (Crank 1975). Fitting the data from Figure 6 of Higashino et al. (2019) to Equation 13 gives
662 logDt (m^2) = –7.4±0.2 (assuming symmetrical uncertainties in log$D$ space). At 800 °C (Higashino
663 et al. 2019) our overall regression for the slow diffusivity gives log$D$ (m^2s^{-1}) of –22.9±0.5 (2σ)
664 resulting in times of 30-320 M.y..

665 Finally, Vielzeuf et al. (2005) reported $\delta^{18}O$ profiles in garnets from migmatitic rocks from the
666 French Pyrenees. As with the data from Higashino et al. (2019), the profile lengths were non-
667 negligible relative to the size of the garnets, thus the spherical model (Equation 13) was applied.
668 At 850 °C (see Vielzeuf et al. 2005), log$D$ = –22.2±0.4, and fitting their data to Equation 13 gives
669 a mean logDt (m^2) of –7.5±0.3, which then results in times between 4 and 50 M.y..

670 The relatively large uncertainty on time in each case comes from (1) the uncertainty on the fit,
671 which is due to the relatively sparse data density as well as the uncertainties on individual points;
672 (2) the uncertainty on D at a given temperature. Although the timescales calculated using our new

673 Arrhenius relationship are comparable to those estimated in the original studies, it is important to
674 be able to reproduce older datasets that estimated metamorphic timescales using an earlier
675 Arrhenius relationship based on limited and unpublished SIMS data by Coghlan (1990,
676 unpublished data).
677
678 **IMPLICATIONS**
679 This study applied a variety of experimental and analytical techniques to investigate oxygen
680 diffusivity in YAG and pyrope garnet at *P-T* conditions varying from 1 atm to 2.5 GPa and from
681 900 to 1600 °C, under both nominally dry and wet conditions. Diffusion profiles measured with
682 SHRIMP, CAMECA IMS-1280 and NanoSIMS are overall consistent in most experimental
683 charges (with the exception of those annealed at HP in hydrothermal conditions). Nevertheless,
684 CAMECA 1280 and NanoSIMS have a higher spatial resolution than SHRIMP in line-scan mode
685 due to the much smaller size of the analyzed domain (<3 μm vs. ~10 × 15 μm), which allowed
686 identifying the complex shapes of the diffusion profiles. Additionally, even though profiles
687 measured in depth-profiling mode by SHRIMP and CAMECA 1280 gave comparable estimates
688 of the first-order approximations for diffusion coefficients, SHRIMP depth profiles could not be
689 fitted using the reaction-diffusion model due to their longer tails resulting from analytical
690 artifacts (edge effects) unavoidable with this instrument. The new data are self-consistent and
691 suggest no significant effect of chemical composition and pressure on oxygen diffusivity, within
692 the uncertainty of the data, and predict slower diffusivity of oxygen relative to major divalent
693 cations when extrapolated to typical crustal *P-T* conditions. Additionally, the data of Coghlan
694 (1990 unpublished data) agree well with the new dataset presented in this study. The complexity
695 of most measured diffusion profiles is interpreted as the result of two different diffusion
696 mechanisms that differ by ~2 log units. The slow mechanism seems prevalent in garnet with

697 natural compositions, hence it may be useful to consider the extent to which O isotopic signatures
698 can be retained as a function of various *T*-*t* conditions.
699 We consider a case in which garnet crystals (assumed spherical) have a homogeneous isotopic
700 signature (C_0), then are exposed to some other isotopic condition at their boundary (C_1) whilst
701 maintaining their shape and size. Equations A2-19 to A2-21 given in Electronic Appendix 2
702 (equivalent to Equations 6.18-6.20 from Crank 1975), are useful for considering retention in
703 spherical systems. Figure 12 shows some example applications considering the effect of
704 temperature, radius and time applying the diffusivities for the slow diffusion mechanism from
705 Equation 11.
706 Whilst these curves do not include the uncertainties associated with the Arrhenius relationship,
707 the models show the utility of O in garnet. Firstly, relevant for using O isotopes in garnet as a
708 geochemical tracer, the core isotopic compositions will almost always be preserved at realistic *T*-*t*
709 conditions. Secondly, whilst subject to uncertainties both in terms of diffusivities and diffusion
710 mechanisms, O in garnet has the potential to be a 'Goldilocks' system for diffusion chronometry
711 in metamorphic systems – neither too fast to eliminate heterogeneities nor too slow for diffusion
712 profiles to be measured given current analytical limitations. Potentially, calibrating O diffusion
713 against major element diffusion in garnets using natural diffusion profiles has promise for
714 increasing confidence in (and potentially refining) the experimental calibration, but we note that,
715 as with O, the extrapolation of major element diffusivities to relevant temperatures also comes
716 with non-negligible uncertainties.
717

FUNDING

This work was supported by the Australian Research Council (grant number DP110101599) and the Swiss National Science Foundation (grant number SNSF 200021_166280) to D.R. M.R.S. and J.W.V. are funded by the U.S. Department of Energy, Office of Science, Office of Basic Energy Sciences under Award Numbers DE-FG02-93ER14389 and DE-SC0020666. WiscSIMS is supported by the U.S. National Science Foundation (EAR-1658823) and the University of Wisconsin-Madison.

ACKNOWLEDGEMENTS

We thank Dean Scott, David Clark and David Cassar for technical assistance during the experiments; Peter Holden, Janaina Avila and Peter Lanc for assistance with SHRIMP. Hugh O'Neill, Eleanor Mare and Johanna Sommer are acknowledged for their feedback with experiments. Harri Kokkonen and Drae Rogers helped with sample preparation at ANU and UW-Madison; Susanne Seitz (University of Lausanne) assisted with sample preparation for NanoSIMS analyses. Mike Spicuzza, Bil Schneider and Kouki Kitajima (UW-Madison) are acknowledged for assistance with laser fluorination analyses, SEM imaging and SIMS analyses in the WiscSIMS lab. Julien Reynes (University of Bern) helped with Monte Carlo simulations. Peter Williams (Arizona State University), Morgan Williams (ANU), Elias Bloch (University of Lausanne), José Alberto Padrón-Navarta and Catherine Thoraval (University of Montpellier) are thanked for constructive discussions. We thank Ralf Dohmen and Weiran Li for constructive reviews. All authors declare no conflicts of interest.

742 **REFERENCES**

743 Ague, J.J., and Carlson, W.D. (2013) Metamorphism as garnet sees it: The kinetics of nucleation
744 and growth, equilibration, and diffusional relaxation. Elements, 9, 439–445.
745 doi:10.2113/gselements.9.6.439

746 Akella, J., Vaidya, S.N., and Kennedy, G.C. (1969) Melting of sodium chloride at pressures to 65
747 kbar. Physical Review, 185, 1135–1140. doi:10.1103/PhysRev.185.1135

748 Avni, Y. (1976) Energy spectra of X-ray clusters of galaxies. The Astrophysical Journal, 210,
749 642–646.

750 Baxter, E.F., Caddick, M.J., and Ague, J.J. (2013) Garnet: Common mineral, uncommonly
751 useful. Elements, 9, 415–419. doi:10.2113/gselements.9.6.415

752 Borinski, S.A., Hoppe, U., Chakraborty, S., Ganguly, J., and Bhowmik, S.K. (2012)
753 Multicomponent diffusion in garnets I: General theoretical considerations and experimental
754 data for Fe-Mg systems. Contribution to Mineralogy and Petrology, 164, 571–586.
755 doi:10.1007/s00410-012-0758-0

756 Caddick, M.J., and Kohn, M.J. (2013) Garnet: Witness to the evolution of destructive plate
757 boundaries. Elements, 9, 427–432. doi:10.2113/gselements.9.6.427

758 Chakraborty, S. (2008) Diffusion in solid silicates: a tool to track timescales of processes comes
759 of age. Annual Review of Earth and Planetary Sciences, 36, 153–190.

760 Chakraborty, S., and Ganguly, J. (1992) Cation Diffusion in Aluminosilicate Garnets:
761 Experimental Determination in Spessartine-Almandine Diffusion Couples, Evaluation of
762 Effective Binary Diffusion Coefficients, and Applications. Contribution to Mineralogy and
763 Petrology, 111, 74–86.

764 Cherniak, D.J., Hervig, R., Koepke, J., Zhang, Y., and Zhao, D. (2010) Analytical Methods in
765 Diffusion Studies. Reviews in Mineralogy and Geochemistry, 72, 107–170.

766 doi:10.2138/rmg.2010.72.4
767 Cockayne, B. (1985) The uses and enigmas of the Al_2O_3-Y_2O_3 phase system. Journal of the Less
768 Common Minerals, 114, 199–206.
769 Coghlan, R.A.N. (1990) Studies in diffusional transport: Grain boundary transport of oxygen in
770 feldspars, diffusion of oxygen, strontium, and the REEs in garnet, and thermal histories of
771 granitic intrusions in south-central Maine using oxygen isotopes. 251 p. Ph.D. thesis, Brown
772 University. Available from https://www.proquest.com/docview/303802606 (13 May 2021) or
773 University Microfilms International (https://www.worldcat.org/title/studies-in-diffusion-
774 transport-grain-boundary-transport-of-oxygen-in-feldspars-diffusion-of-oxygen-strontium-
775 and-the-rees-in-garnet-and-thermal-histories-of-granitic-intrusions-in-south-central-maine-
776 using-oxygen-isotopes/oclc/31422529&referer=brief_results; 13 May 2021).
777 Connolly, J.A.D., and Cesare, B. (1993) C-O-H-S fluid composition and oxygen fugacity in
778 graphitic metapelites. Journal of Metamorphic Geology, 11, 379–388.
779 Costa, F., and Chakraborty, S. (2008) The effect of water on Si and O diffusion rates in olivine
780 and implications for transport properties and processes in the upper mantle. Physics of the
781 Earth and Planetary Interiors, 166, 11–29. doi:10.1016/j.pepi.2007.10.006
782 Crank, J. (1975) The Mathematics of Diffusion, 421 p. Clarendon, Oxford.
783 Crowe, D.E., Riciputi, L.R., Bezenek, S., and Ignatiev, A. (2001) Oxygen isotope and trace
784 element zoning in hydrothermal garnets: Windows into large-scale fluid-flow behavior.
785 Geology, 29, 479–482.
786 D'Errico, M.E., Lackey, J.S., Surpless, B.E., Loewy, S.L., Wooden, J.L., Barnes, J.D.,
787 Strickland, A., and Valley, J.W. (2012) A detailed record of shallow hydrothermal fluid flow
788 in the sierra nevada magmatic arc from low-$\delta^{18}O$ skarn garnets. Geology, 40, 763–766.
789 doi:10.1130/G33008.1

790 Dohmen, R., Becker, H.W., Meissner, E., Etzel, T., and Chakraborty, S. (2002) Production of
791 silicate thin films using pulsed laser deposition (PLD) and applications to studies in mineral
792 kinetics. European Journal of Mineralogy, 14, 1155–1168. doi:10.1127/0935-1221/2002/0014-
793 1155
794 Dohmen, R., Kasemann, S.A., Coogan, L., and Chakraborty, S. (2010) Diffusion of Li in olivine.
795 Part I: Experimental observations and a multi species diffusion model. Geochimica et
796 Cosmochimica Acta, 74, 274–292. doi:10.1016/j.gca.2009.10.016
797 Eiler, J.M., Valley, J.W., and Baumgartner, L.P. (1993) A new look at stable isotope
798 thermometry. Geochimica et Cosmochimica Acta, 57, 2571–2583.
799 Errico, J.C., Barnes, J.D., Strickland, A., and Valley, J.W. (2013) Oxygen isotope zoning in
800 garnets from Franciscan eclogite blocks: Evidence for rock-buffered fluid interaction in the
801 mantle wedge. Contribution to Mineralogy and Petrology, 166, 1161–1176.
802 doi:10.1007/s00410-013-0915-0
803 Freer, R., and Dennis, P.F. (1982) Oxygen diffusion studies I: A preliminary ion microprobe
804 investigation of oxygen diffusion in some rock-forming minerals. Mineralogical Magazine,
805 45, 179–192.
806 Freer, R., and Edwards, A. (1999) An experimental study of Ca-(Fe,Mg) interdiffusion in silicate
807 garnets. Contribution to Mineralogy and Petrology, 134, 370–379.
808 doi:10.1007/s004100050491
809 Ganguly, J. (2010) Cation diffusion kinetics in aluminosolicate garnets and geological
810 applications. Reviews in Mineralogy and Geochemistry, 72, 559–601.
811 Ganguly, J., Cheng, W., and Chakraborty, S. (1998) Cation diffusion in aluminosilicate garnets:
812 Experimental determination in pyrope-almandine diffusion couples. Contribution to
813 Mineralogy and Petrology, 131, 171–180. doi:10.1007/s004100050386

814 Gauthiez-Putallaz L., Nutman, A.P., Bennett, V.C., and Rubatto, D. (2020) Tracking heavy $\delta^{18}O$
815 signatures in 3.7-3.6 Ga crust: a zircon and garnet record in Isua clastic metasedimentary
816 rocks. Chemical Geology, 537, 119474 doi:doi.org/10.1016/j.chemgeo.2020.119474
817 Gérard, O., and Jaoul, O. (1989) Oxygen diffusion in San Carlos olivine. Journal of Geophysical
818 Research, 94, 4119–4128.
819 Gibbs, G.V., and Smith, J.V. (1965) Refinement of the crystal structure of synthetic pyrope.
820 American Mineralogist, 50, 2023–2039.
821 Giletti, B.J., Semet, M.P., and Yund, R.A. (1978) Studies in diffusion III. Oxygen in feldspar: an
822 ion microprobe determination. Geochimica et Cosmochimica Acta, 42, 45–46.
823 Hack, A.C., and Mavrogenes, J.A. (2006) A cold-sealing capsule design for synthesis of fluid
824 inclusions and other hydrothermal experiments in a piston-cylinder apparatus. American
825 Mineralogist, 91, 203–210. doi:10.2138/am.2006.1898
826 Haneda, H., Miyazawa, Y., and Shirasaki, S. (1984) Oxygen Diffusion in Single Crystal Yttrium
827 Aluminum Garnet. Journal of Crystal Growth, 68, 581–588.
828 He, Q., Zhang, S.-B., Zheng, Y.-F., Xia, Q.-X., and Rubatto, D. (2019) Geochemical evidence for
829 hydration and dehydration of crustal rocks during continental rifting. Journal of Geophysical
830 Research – Solid Earth 124, 12593–12619. doi: https://doi.org/10.1029/2019JB018508
831 Hermann, J., Troitzsch, U., and Scott, D. (2016) Experimental subsolidus phase relations in the
832 system $CaCO_3$–$CaMg(CO_3)_2$ up to 6.5 GPa and implications for subducted marbles. Contribution to
833 Mineralogy and Petrology, 171, 1–17.
834 Higashino, F., Rubatto, D., Kawakami, T., Bouvier, A.-S., and Baumgartner, L.P. (2019) Oxygen
835 isotope speedometry in granulite facies garnet recording fluid/melt-rock interaction (Sør
836 Rondane Mountains, East Antarctica). Journal of Metamorphic Geology, 37, 1037–1048
837 doi:10.1111/jmg.12490

838 Hofmann, S. (2000) Ultimate depth resolution and profile reconstruction in sputter profiling with
839 AES and SIMS. Surface and Interface Analysis, 30, 228–236.
840 Hofmann, S. (2014) Sputter depth profiling: Past, present, and future. Surface and Interface
841 Analysis, 46, 654–662. doi:10.1002/sia.5489
842 Hoppe, P., Cohen, S., and Meibom, A. (2013) NanoSIMS: Technical Aspects and Applications in
843 Cosmochemistry and Biological Geochemistry. Geostandards and Geoanalytical Research, 37,
844 111–154. doi:10.1111/j.1751-908X.2013.00239.x
845 Ireland, T.R., Clement, S., Compston, W., Foster, J.J., Holden, P., Jenkins, B., Lanc, P., Schram,
846 N., and Williams, I.S. (2008) Development of SHRIMP. Australian Journal of Earth Sciences,
847 55, 937–954. doi:10.1080/08120090802097427
848 Jain, A., Ong, S.P., Hautier, G., Chen, W., Richards, W.D., Dacek, S., Cholia, S., Gunter, D.,
849 Skinner, D., Ceder, G., and Persson, K.A. (2013) Commentary: The materials projects: A
850 materials genome approach to accelerating materials innovation. APL Materials, 1, 011002.
851 Jollands, M.C., Padrón-Navarta, J.A., Hermann, J., and O'Neill, H.St.C. (2016a) Hydrogen
852 diffusion in Ti-doped forsterite and the preservation of metastable point defects. AMerican
853 Mineralogist, 101, 1571–1583.
854 Jollands, M.C., Hermann, J., O'Neill, H.St.C., Spandler, C., and Padrón-Navarta, J.A. (2016b)
855 Diffusion of Ti and some divalent cations in olivine as a function of temperature, oxygen
856 fugacity, chemical potentials and crystal orientation. Journal of Petrology, 57, 1983–2010.
857 doi:10.1093/petrology/egw067
858 Kilburn, M.R. and Wacey, D. (2014) CHAPTER 1:Nanoscale Secondary Ion Mass Spectrometry
859 (NanoSIMS) as an Analytical Tool in the Geosciences, in *Principles and Practice of*
860 *Analytical Techniques in Geosciences*, p. 1–34 doi: 10.1039/9781782625025-00001
861 Kita, N.T., Ushikubo, T., Fu, B., and Valley, J.W. (2009) High precision SIMS oxygen isotope

862 analysis and the effect of sample topography. Chemical Geology, 264, 43–57.
863 doi:10.1016/j.chemgeo.2009.02.012
864 Kohn, M.J., Valley, J.W., Elsenheimer, D., and Spicuzza, M.J. (1993) O isotope zoning in garnet
865 and staurolite: Evidence for closed-system mineral growth during regional metamorphism.
866 American Mineralogist, 78, 988–1001.
867 Lasaga, A.C. (1979) Multicomponent exchange and diffusion in silicates. Geochimica et
868 Cosmochimica Acta, 43, 455-468.
869 Li, Z., Liu, B., Wang, J., Sun, L., Wang, J., and Zhou, Y. (2012) Mechanism of Intrinsic Point
870 Defects and Oxygen Diffusion in Yttrium Aluminum Garnet: First-Principles Investigation.
871 Journal of the American Ceramic Society, 95, 3628–3633.
872 Martin, L.A.J., Rubatto, D., Crépisson, C., Hermann, J., Putlitz, B., and Vitale-Brovarone, A.
873 (2014) Garnet oxygen analysis by SHRIMP-SI: Matrix corrections and application to high-
874 pressure metasomatic rocks from Alpine Corsica. Chemical Geology, 374–375, 25–36.
875 doi:10.1016/j.chemgeo.2014.02.010
876 Moy, A., and Fournelle, J. (2017) Analytical Spatial Resolution in EPMA: What is it and how
877 can it be estimated? Microscopy and Microanalysis, 23 (Suppl 1).
878 doi:10.1017/S1431927617006158
879 Novak, G.A., Gibbs, G.V. (1971) The crystal chemistry of the silicate garnets. American
880 Mineralogist, 56, 791–825
881 Page, F.Z., Kita, N.T., and Valley, J.W. (2010) Ion microprobe analysis of oxygen isotopes in
882 garnets of complex chemistry. Chemical Geology, 270, 9–19.
883 doi:10.1016/j.chemgeo.2009.11.001
884 Page, F.Z., Essene, E.J., Mukasa, S.B., and Valley, J.W. (2014) A garnet-zircon oxygen isotope
885 record of subduction and exhumation fluids from the Franciscan complex, California. Journal

of Petrology, 55, 103–131. doi:10.1093/petrology/egt062

Pownceby, M.I., and O'Neill, H.St.C. (1994) Thermodynamic data from redox reactions at high temperatures. IV. Calibration of the Re-ReO_2 oxygen buffer from EMF and NiO+Ni-Pd redox sensor measurements. Contribution to Mineralogy and Petrology, 118, 130–137.

Press, W.H., Teukolsky, S.A., Vetterling, W.T., and Flannery, B.P. (2007) Numerical Recipes 3rd Edition, The Art of Scientific Computing, 1256 p., Cambridge University Press.

Reynes, J., Jollands, M., Hermann, J., and Ireland, T. (2018) Experimental constraints on hydrogen diffusion in garnet. Contribution to Mineralogy and Petrology, 173, 1–23. doi:10.1007/s00410-018-1492-z

Rubatto, D., and Angiboust, S. (2015) Oxygen isotope record of oceanic and high-pressure metasomatism: a P–T–time–fluid path for the Monviso eclogites (Italy). Contribution to Mineralogy and Petrology, 170, 1–16.

Russell, A.K., Kitajima, K., Strickland, A., Medaris, L.G., Schulze, D.J., and Valley, J.W. (2013) Eclogite-facies fluid infiltration: Constraints from $\delta^{18}O$ zoning in garnet. Contribution to Mineralogy and Petrology, 165, 103–116. doi:10.1007/s00410-012-0794-9

Ryerson, F.J., Durham, W.D., Cherniak, D.J., and Lanford, W.A. (1989) Oxygen diffusion in olivine: effect of oxygen fugacity and implications for creep. Journal of Geophysical Research, 94, 4105–4118.

Sakaguchi, I., Haneda, H., and Tanaka J. (1996) Effect of Composition on the Oxygen Tracer Diffusion in Transparent Yttrium Aluminium Garnet (YAG) Ceramics. Journal of the American Ceramic Society, 79, 1627–1632.

Skelton, A., Annersten, H., and Valley, J. (2002) $\delta^{18}O$ and yttrium zoning in garnet: Time markers for fluid flow? Journal of Metamorphic Geology, 20, 457–466. doi:10.1046/j.1525-1314.2002.00378.x

910 Sobolev, N.V., Schertl, H.P., Valley, J.W., Page, F.Z., Kita, N.T., Spicuzza, M.J., Neuser, R.D.,
911 and Logvinova, A.M. (2011) Oxygen isotope variations of garnets and clinopyroxenes in a
912 layered diamondiferous calcsilicate rock from Kokchetav Massif, Kazakhstan: A window into
913 the geochemical nature of deeply subducted UHPM rocks. Contribution to Mineralogy and
914 Petrology, 162, 1079–1092. doi:10.1007/s00410-011-0641-4
915 Tollan, P.M., O'Neill, H.St.C., and Hermann, J. (2018) The role of trace elements in controlling
916 H incorporation in San Carlos olivine. Contribution to Mineralogy and Petrology, 173,
917 doi.org/10.1007/s00410-018-1517-7
918 Valley, J.W. (2001) Stable isotope thermometry at high temperatures. Reviews in Mineralogy
919 and Geochemistry, 43, 365–413.
920 Valley, J.W., Kitchen, N., Kohn, M.J., Niendorf, C.R. and Spicuzza, M.J. (1995) UWG-2, a
921 garnet standard for oxygen isotope ratios: Strategies for high precision and accuracy with laser
922 heating. Geochimica et Cosmochimica Acta, 59, 5223–5231.
923 Van Orman, J.A., Grove, T.L., Shimizu, N. (2001) Rare earth element diffusion in diopside:
924 influence of temperature, pressure, and ionic radius, and an elastic model for diffusion in
925 silicates. Contribution to Mineralogy and Petrology, 141, 687–703.
926 Van Orman, J.A., Grove, T.L., Shimizu, N., and Layne, G.D. (2002) Rare earth element diffusion
927 in a natural pyrope single crystal at 2.8 GPa. Contribution to Mineralogy and Petrology, 142,
928 416–424. doi:10.1007/s004100100304
929 Van Orman, J.A., Li, C., and Crispin, K.L. (2009) Aluminum diffusion and Al-vacancy
930 association in periclase. Physics of the Earth and Planetary Interiors, 172, 34–42.
931 doi:10.1016/j.pepi.2008.03.008

Van Orman, J.A., Cherniak, D.J., and Kita, N.T. (2014) Magnesium diffusion in plagioclase: dependence on composition, and implications for thermal resetting of the ^{26}Al-^{26}Mg early solar system chronometer. Earth and Planetary Science Letters, 385, 79-88.

Vielzeuf, D., Veschambre, M., and Brunet, F. (2005) Oxygen isotope heterogeneities and diffusion profile in composite metamorphic-magmatic garnets from the Pyrenees. American Mineralogist, 90, 463–472. doi:10.2138/am.2005.1576

Vielzeuf, D., Baronnet, A., Perchuk, A.L., Laporte, D., and Baker, M.B. (2007) Calcium diffusivity in alumino-silicate garnets: An experimental and ATEM study. Contribution to Mineralogy and Petrology, 154, 153–170. doi:10.1007/s00410-007-0184-x

Vho, A., Rubatto, D., Lanari, P., Giuntoli, F., Regis, D., and Hermann, J. (2020) Crustal reworking and hydration: Insights from element zoning and oxygen isotopes of garnet in high-pressure rocks (Sesia Zone, Western Alps, Italy). Contribution to Mineralogy and Petrology, doi:10.1007/s00410-020-01745-6

Warshaw, I., and Roy, R. (1959) Stable and Metastable Equilibria in the Systems Y_2O_2-Al_2O_3, and Gd_2O_3-Fe_2O_3. Journal of the American Ceramic Society, 42, 434–438.

Zhang, Y., and Cherniak, D.J. (2010) Diffusion in minerals and melts: introduction. Reviews in Mineralogy and Geochemistry, 72, 1–4.

Zheng, Y.F., and Fu, B. (1998) Estimation of oxygen diffusivity from anion porosity in minerals. Geochemical Journal, 32, 71–89. doi:10.2343/geochemj.32.71

Zinner, E. (1980) Depth profiling by secondary ion mass spectrometry. Scanning, 3, 57–78. doi:10.1002/sca.4950030202

FIGURE CAPTIONS

Figure 1. Images of YAG annealed in a gas mixing furnace at (**a**) 1450 °C (failed experiment not discussed in the text) where it is possible to see the ^{18}O-enriched YAG+Crn buffer sintered on top of the crystal (reflected light). (**b**) Sketch showing sample preparation for line-scan analysis by SIMS (see text for details). (**c**) Reflected light image of a line-scan measurement for δ^{18}O with SHRIMP (sample YLPD-1; T = 1600 °C, P = 1 atm). Analyses were performed obliquely to the diffusion interface to increase the number of spots within the diffusion profile. SEM-BSE (**d**) and CL (**e**) images of a line-scan measurement performed with a CAMECA IMS-1280 (sample YLPD-1).

Figure 2. Images of garnet crystals recovered from HP experiments. Reflected light images of YAG sample YHPW-1 (**a**) and Prp-1 sample PHPW-1 (**b**) annealed at 900 °C and 1.0 GPa for 14 days under water-present conditions, mounted in epoxy discs for forward depth profiling analysis by SIMS. The buffer recrystallized on top of the original interface in both pyrope and YAG. Reflected light images of YAG crystals annealed at 1.5 GPa under nominally dry conditions at 1300 °C (sample YHPD-5) (**c**) and 1500 °C (sample YHPD-8) (**d**). Crystals are surrounded by the graphite+^{18}O-enriched YAG+Crn powder. Two line-scan measurements by SHRIMP are visible in (**d**). SEM-BSE (**e**) and CL (**f**) images of line-scan measurements performed with a CAMECA IMS-1280 in the same sample (YHPD-8). Images in (**e**) and (**f**) are rotated by 90° relative to image in (**d**).

Figure 3. (**a**) SEM-BSE image of a line-scan analysis conducted with a NanoSIMS in YAG annealed at 1400 °C and 1.5 GPa under nominally anhydrous conditions for 95.5 h (sample YHPD-6). (**b**) SEM X-ray map of the same crystal. Both images show that the diffusion interface is well preserved.

Figure 4. Concentration-distance profiles with error function geometry measured in line-scan

mode by SHRIMP and CAMECA IMS-1280 in YAG annealed in a gas mixing furnace (P = 1 atm) at 1600 °C (sample YLPD-1). The large uncertainty on the distance in the profile measured by SHRIMP is due to the relatively large size of the SHRIMP pit (~10 × 15 μm) vs. ~3 μm for the IMS-1280. The measured profiles were fitted to Equation 1 by using the least squares regression. Error bars for $^{18}O/(^{18}O+^{16}O)$ ratios are not visible because smaller than the symbols.

Figure 5. 'Stepped' concentration-distance profiles measured in YAG annealed under nominally anhydrous conditions at (**a, b**) 1400 °C and 1.5 GPa, (**c, d**) 1200 °C and 1.5 GPa, (**e**) 1600 °C and 1.5 GPa. Two experiments were performed for different durations (numbers on curves) at both 1400 °C and 1200 °C to ensure no time-dependence of oxygen diffusivity and to compare results obtained in line-scan mode with the NanoSIMS (**a, c**) and in depth profiling mode by IMS-1280 (**b**) and SHRIMP (**d**). The profiles can be divided into two to three zones (I, II, III; see text for details). (**e**) The lower spatial resolution of the line-scan analysis by SHRIMP did not allow the identification of the complex features in the concentration-distance profiles, in contrast to line-scan analysis with a NanoSIMS performed in the same sample. However, the penetration distances are comparable. Error bars for $^{18}O/(^{18}O+^{16}O)$ ratios are not visible because smaller than the symbols.

Figure 6. Arrhenius plot showing approximate average values of $\widetilde{D}$ (for complexly shaped profiles) and D (for profiles with error-function form) in garnet calculated in this study by fitting profiles to Equation 1 (log$\widetilde{D}$s calculated from SHRIMP depth profiling at 900 °C are not used to determine this Arrhenius relationship, see text; Table 2). The different symbols indicate the various analytical methods used to measure the concentration-distance profiles. $\widetilde{D}$s and Ds calculated from multiple profiles measured with different techniques in the same experimental charge, or in different experimental charges annealed under similar P-T conditions, are

comparable within uncertainty. The different colors indicate the different *P* at which both YAG and pyrope were annealed, whereas the fill indicates either presence (empty symbols) or absence (full symbols) of a free fluid (H_2O) phase. Oxygen isotope data for each diffusion profile measured in this study are shown in Tables S3 to S5 (electronic supplement). Samples with error-function shaped profiles are: YLPD-1, YLPD-2, YHPD-1 and PHPW-1.

Figure 7. Examples of measured profiles from nominally dry (**a, b**) and wet (**c, d**) experiments along with the associated model fits, and the concentrations of all modelled species. Note the difference in *x* axes on the different panels – similar behavior is observed at very different spatial scales. Experiments: a) YHPD-5 (T = 1300 °C, P = 1.5 GPa, t = 218 h), b) YHPD-2 (T = 1200 °C, P = 1.5 GPa, t = 48 h), c) PHPW-1 (T = 900 °C, P = 1.0 GPa, t = 366 h), d) YHPW-3 (T = 900 °C, P = 1.5 GPa, t = 336 h).

Figure 8. (**a**) Arrhenius plot showing values of oxygen diffusion coefficients (*D)* in garnet calculated in this study by fitting profiles to Equation 1 (for error-function shaped profiles) and to the diffusion-reaction model (for complexly shaped profiles). See text for details. The same diffusion coefficients are shown in (**b**) according to the analytical method used to acquire the $^{18}O/(^{18}O+^{16}O)$ profiles. The figure only includes the Coghlan (1990 unpublished data) data from his longest experimental runs, i.e. the profiles least affected by analytical artifacts. This is following the decision of Coghlan (see his Table 2.2 and Fig. 2.3.a).

Figure 9. Variations in profile shapes due to (**a**) changing the interface ^{18}O concentration and (**b**) changing *K*. Models in both (**a**) and (**b**) were run with the following parameters: $\sum X_O$ (initial and interface): 0.35; $\sum^{18}O$ (initial): 0.025; $D^{18}O_i''$=10^{-17} m^2s^{-1}; $D^{18}O_O^{\times} = DV_O^{\bullet\bullet}$=$10^{-19}$ m^2s^{-1}. In (**a**), $^{18}O/(^{18}O+^{16}O)$ was varied between 0.005 and 0.15 – the values on the *y*-axis are given in ^{18}O per 12xO; and in (**b**) log*K* was varied between -1 and 3.

Figure 10. Comparison of the Arrhenius relations determined in this study with previous

experimental calibrations for (**a**) oxygen and (**b**) major cations in garnet. Data for cations are normalized to a pressure of 1 GPa using the activation volumes ($Jbar^{-1}mol^{-1}$) calculated by Chakraborty and Ganguly (1992) for Mg, Mn and Fe. Because no experimental data on the pressure dependence of D_{Ca} is available, an activation volume of 0.6 $Jbar^{-1}mol^{-1}$ was assumed for Ca, according to Ganguly (2010). Data are not normalized to a fixed oxygen fugacity. CG92: Chakraborty and Ganguly (1992); G98: Ganguly et al. (1998); FE99: Freer and Edwards (1999); V07: Vielzeuf et al. (2007); B12: Borinski et al. (2012).

Figure 11. Data from three studies, described in the text, fitted to Equations 12 or 13. 2σ uncertainties on the fits are estimated as minimum chi-square+4 that of the same associated with the best fit (i.e. based on the 'constant chi-square boundaries' method from Press et al. 2007).

Figure 12. Some examples considering the retentivity of O isotopic signatures at different *T*-*t* conditions. (**a**): the bulk garnet composition, given as the difference between the original and imposed boundary composition, as a function of radius at 800 °C (Equation A2.19, Electronic Appendix 2). (**b**) The evolution of a profile, in spherical coordinates, as a function of time. The curves represent times of 1, 10, 100, 200, 500, 1000 and 2000 M.y. (Equation A2.20, Electronic Appendix 2). (**c**) As (**a**), but considering the core of a garnet crystal of different radii, rather than its bulk signature (Equation A2.21, Electronic Appendix 2). (**d**) The time taken to modify the bulk composition of a garnet to a value of 0.5 (i.e. midway between the initial and boundary compositions) as a function of temperature and radius.

SUPPLEMENTARY FIGURE AND TABLE CAPTIONS

Figure S1. Histograms of spacing between oxygen ions in YAG, pyrope, almandine and spessartine derived from X-ray diffraction data, and tabulated by CrystalMakerX software. Bins represent a range of 0.05 Å. Data sources: YAG: Jain et al. (2013); pyrope: Gibbs and Smith

(1965); almandine, spessartine: Novak and Gibbs (1971).

Figure S2. Schematic illustration of experimental assemblies for wet (**a**) and nominally dry (**b**) HP experiments. See text for details.

Figure S3. Schematic illustration of a cold-sealed Ag capsule used for HP experiments under water-present conditions (**a**), a 3.5 mm Pt capsule (**b**), and graphite-lined platinum capsules used for nominally anhydrous HP experiments (**c**). See text for details.

Figure S4. Oxygen diffusivity in garnet as a function of pressure determined at different temperatures and under both wet and nominally dry conditions. See text for details.

Table S1. Representative major element compositions (wt.%) by EPMA of synthetic YAG used for the experiments. Cations are based on 12 oxygens.

Table S2. Representative major element compositions (wt.%) by EDXA-SEM of natural garnet crystals used for the experiments. Cations are based on 12 oxygens.

Table S3. Complete data table of oxygen isotope measurements done in experimental charges of YAG annealed at 1500 or 1600 °C and 1 atm in a gas mixing furnace, along with images of each traverse.

Table S4. Complete data table of oxygen isotope measurements done in experimental charges of YAG or pyrope annealed at 900 °C and 1.0 or 1.5 GPa under water-saturated conditions, along with images of each SIMS pit.

Table S5. Complete data table of oxygen isotope measurements done in experimental charges of YAG annealed at 1050, 1200, 1300, 1400, 1500 or 1600 °C and 1.5 or 2.5 GPa under nominally dry conditions, along with images of each SIMS pit and traverse.

Table S6. Estimate of depth resolution during depth profiling by CAMECA IMS-1280 and by SHRIMP. Analyses were performed in YAG reference material coated with an olivine thin film enriched in ^{18}O.

Table 1. Temperature, pressure, and time conditions for successful experiments conducted in gas mixing furnace and end-loaded piston cylinder apparatus under both wet and nominally anhydrous conditions.

Experiment ID*	Garnet	*T* (°C)	*P*	*t* (hours)	^{18}O-buffer	Free fluid phase
YLPD-1	YAG	1600	1 atm	24	^{18}O-enriched(YAG+Crn)	no
YLPD-2	YAG	1500	1 atm	168	^{18}O-enriched(YAG+Crn)	no
YHPW-1	YAG	900	1.0 GPa	336	YAG+Crn+^{18}O-rich H_2O	yes
YHPW-2	YAG	900	1.0 GPa	262	YAG+Crn+^{18}O-rich H_2O	yes
YHPW-3	YAG	900	1.5 GPa	336	YAG+Crn+^{18}O-rich H_2O	yes
PHPW-1	Prp-1	900	1.0 GPa	336	Prp-1+^{18}O-rich H_2O	yes
YHPD-1	YAG	1050	1.5 GPa	240	^{18}O-enriched(YAG+Crn)+Gr	no
YHPD-2	YAG	1200	1.5 GPa	48	^{18}O-enriched(YAG+Crn)+Gr	no
YHPD-3	YAG	1200	1.5 GPa	240	^{18}O-enriched(YAG+Crn)+Gr	no
YHPD-4	YAG	1200	1.5 GPa	24	^{18}O-enriched(YAG+Crn)+Gr	no
YHPD-5	YAG	1300	1.5 GPa	218	^{18}O-enriched(YAG+Crn)+Gr	no
YHPD-6	YAG	1400	1.5 GPa	95.5	^{18}O-enriched(YAG+Crn)+Gr	no
YHPD-7	YAG	1400	1.5 GPa	2	^{18}O-enriched(YAG+Crn)+Gr	no
YHPD-8	YAG	1500	1.5 GPa	144	^{18}O-enriched(YAG+Crn)+Gr	no
YHPD-10	YAG	1600	1.5 GPa	27.5	^{18}O-enriched(YAG+Crn)+Gr	no
YHPD-11	YAG	1500	2.5 GPa	144	^{18}O-enriched(YAG+Crn)+Gr	no

* The notation of the experiment ID indicates the garnet composition (P = pyrope, Y = YAG), the pressure (LP = 1-atm experiments, HP = piston cylinder experiments) and the presence/absence of water (W = wet, D = dry).

1081 **Table 2.** Oxygen diffusion coefficients (m^2s^{-1}) calculated in YAG and pyrope according to the

1082 error-function fit (erf fit) and diffusion-reaction model (diff-reac).

Experiment ID	Garnet	T (°C)	P	t (h)	$\log_{10}D$ erf fit (Eq. 1)	$\log_{10}D$ $^{18}O_i''$ diff-reac	$\log_{10}D$ $V_O^{\bullet\bullet}$ diff-reac	$\log_{10}D$ $O_O^{\times}$ diff-reac	Analytical method
YHPW-1_s1	YAG	900	1.0 GPa	336	-19.6				SHRIMP d.p.
YHPW-1_s2	YAG	900	1.0 GPa	336	-19.6				SHRIMP d.p.
YHPW-1_s3	YAG	900	1.0 GPa	336	-19.6				SHRIMP d.p.
YHPW-1_s4	YAG	900	1.0 GPa	336	-19.7				SHRIMP d.p.
YHPW-1_c1	YAG	900	1.0 GPa	336		*-19.4*	*-21.7*	*-21.7*	CAMECA 1280 d.p.
					-21.8				
YHPW-1_c2	YAG	900	1.0 GPa	336		*-19.5*	*-21.6*	*-21.6*	CAMECA 1280 d.p.
					-21.9				
YHPW-2_s1	YAG	900	1.0 GPa	336	-19.0				SHRIMP d.p.
YHPW-2_s2	YAG	900	1.0 GPa	336	-19.4				SHRIMP d.p.
YHPW-2_s3	YAG	900	1.0 GPa	336	-19.1				SHRIMP d.p.
YHPW-2_s4	YAG	900	1.0 GPa	336	-19.0				SHRIMP d.p.
YHPW-2_c1	YAG	900	1.0 GPa	262	*-20.8*				CAMECA 1280 d.p.
					-21.1				
YHPW-2_c2	YAG	900	1.0 GPa	262	*-20.8*				CAMECA 1280 d.p.
					-21.5				
YHPW-2_c3	YAG	900	1.0 GPa	262	*-21.0*				CAMECA 1280 d.p.
					-21.6				
YHPW-3_s1	YAG	900	1.5 GPa	336	-19.4				SHRIMP d.p.
YHPW-3_c1	YAG	900	1.5 GPa	336		*-19.7*	*-21.7*	*-21.7*	CAMECA 1280 d.p.
					-21.6				
PHPW-1_s1	Prp	900	1.0 GPa	336	-19.2				SHRIMP d.p.
PHPW-1_s2	Prp	900	1.0 GPa	336	-19.2				SHRIMP d.p.
PHPW-1_c1	Prp	900	1.0 GPa	336	-20.5	*-19.1*	*-19.1*	*-22.0*	CAMECA 1280 d.p.
						-19.0	*-20.5*	*-20.5*	
PHPW-1_c2	Prp	900	1.0 GPa	336	*-20.9*				CAMECA 1280 d.p.
					-21.2				
PHPW-1_c3	Prp	900	1.0 GPa	336	*-21.7*				CAMECA 1280 d.p.
					-21.2				
YHPD-1_ns1	YAG	1050	1.5 GPa	240	*-17.4*				NanoSIMS tr.
YHPD-1_ns2	YAG	1050	1.5 GPa	240	*-17.5*				NanoSIMS tr.
YHPD-2_s1	YAG	1200	1.5 GPa	48	-17.8				SHRIMP d.p.
YHPD-2_s2	YAG	1200	1.5 GPa	48	-17.6				SHRIMP d.p.
YHPD-2_c1	YAG	1200	1.5 GPa	48	-18.0	*-17.0*	*-19.4*	*-19.4*	CAMECA 1280 d.p.

s = SHRIMP, c = CAMECA IMS-1280, ns = NanoSIMS, d.p. = depth profiling, tr. = line-scan. For HP wet experiments, two sets of parameters are given depending on the position of the diffusion interface. All values in italics are those defining the two Arrhenius relationships for slow and fast mechanisms. $^{18}O_i''$ = oxygen in interstitial site, $V_O^{\bullet\bullet}$ = oxygen vacancy, $O_O^{\times}$ = oxygen in lattice site.

Experiment ID	Garnet	T (°C)	P	t (h)	$\log_{10}D$ erf fit (Eq. 1)	$\log_{10}D$ $^{18}O_i''$ diff-reac	$\log_{10}D$ $V_O^{\bullet\bullet}$ diff-reac	$\log_{10}D$ $O_O^{\times}$ diff-reac	Analytical method
YHPD-2_c2	YAG	1200	1.5 GPa	48	-18.0	*-16.6*	*-19.9*	*-19.9*	CAMECA 1280 d.p.
YHPD-2_c3	YAG	1200	1.5 GPa	48	-17.9	*-16.8*	*-19.8*	*-19.8*	CAMECA 1280 d.p.
YHPD-3_ns1	YAG	1200	1.5 GPa	240	-17.6	*-16.8*	*-18.9*	*-19.0*	NanoSIMS tr.
YHPD-3_ns2	YAG	1200	1.5 GPa	240	-17.7	*-16.8*	*-19.2*	*-19.2*	NanoSIMS tr.
YHPD-4_s1	YAG	1200	1.5 GPa	24	-17.0				SHRIMP d.p.
YHPD-4_s2	YAG	1200	1.5 GPa	24	-17.0				SHRIMP d.p.
YHPD-4_c1	YAG	1200	1.5 GPa	24	-17.8	*-16.7*	*-19.6*	*-19.7*	CAMECA 1280 d.p.
YHPD-4_c2	YAG	1200	1.5 GPa	24	-17.8	*-16.7*	*-20.0*	*-20.0*	CAMECA 1280 d.p.
YHPD-5_ns1	YAG	1300	1.5 GPa	218	-16.8	*-16.0*	*-19.3*	*-19.3*	NanoSIMS tr.
YHPD-5_ns2	YAG	1300	1.5 GPa	218	-16.8	*-16.0*	*-17.8*	*-18.2*	NanoSIMS tr.
YHPD-6_s1	YAG	1400	1.5 GPa	95.5	-15.8				SHRIMP tr.
YHPD-6_ns1	YAG	1400	1.5 GPa	95.5	-15.5	*-15.2*	*-15.4*	*-17.1*	NanoSIMS tr.
YHPD-7_s1	YAG	1400	1.5 GPa	2	-15.5				SHRIMP d.p.
YHPD-7_s2	YAG	1400	1.5 GPa	2	-15.7				SHRIMP d.p.
YHPD-7_c1	YAG	1400	1.5 GPa	2	-16.1				CAMECA 1280 d.p.
YHPD-7_c2	YAG	1400	1.5 GPa	2	-16.3	*-15.1*	*-17.1*	*-18.2*	CAMECA 1280 d.p.
YHPD-7_c3	YAG	1400	1.5 GPa	2	-16.2	*-15.2*	*-16.8*	*-18.9*	CAMECA 1280 d.p.
YHPD-7_c4	YAG	1400	1.5 GPa	2	-16.2	*-15.3*	*-16.5*	*-16.5*	CAMECA 1280 d.p.
YHPD-7_c5	YAG	1400	1.5 GPa	2	-16.3	*-15.3*	*-16.7*	*-15.6*	CAMECA 1280 d.p.
YHPD-8_s1	YAG	1500	1.5 GPa	144	-14.8				SHRIMP tr.
YHPD-8_s2	YAG	1500	1.5 GPa	144	-14.8				SHRIMP tr.
YHPD-8_c1	YAG	1500	1.5 GPa	144	-14.9	*-14.3*	*-15.5*	*-15.6*	CAMECA 1280 tr.
YHPD-8_c2	YAG	1500	1.5 GPa	144	-14.9	*-14.0*	*-15.8*	*-15.8*	CAMECA 1280 tr.
YHPD-8_c3	YAG	1500	1.5 GPa	144	-14.9	*-14.1*	*-15.7*	*-15.7*	CAMECA 1280 tr.
YHPD-8_c4	YAG	1500	1.5 GPa	144	-14.9	*-14.2*	*-15.6*	*-15.6*	CAMECA 1280 tr.
YHPD-10_s1	YAG	1600	1.5 GPa	27.5	-15.1				SHRIMP tr.
YHPD-10_ns1	YAG	1600	1.5 GPa	27.5	-15.3	*-14.4*	*-16.0*	*-16.0*	NanoSIMS tr.
YHPD-11_s1	YAG	1500	2.5 GPa	144	-15.3				SHRIMP tr.
YHPD-11_s2	YAG	1500	2.5 GPa	144	-15.0				SHRIMP tr.
YHPD-11_c1	YAG	1500	2.5 GPa	144	-15.2	*-14.5*	*-16.2*	*-16.2*	CAMECA 1280 tr.
YHPD-11_c2	YAG	1500	2.5 GPa	144	-15.1	*-14.3*	*-16.2*	*-16.2*	CAMECA 1280 tr.
YHPD-11_c3	YAG	1500	2.5 GPa	144	-15.3	*-14.5*	*-16.0*	*-16.0*	CAMECA 1280 tr.
YHPD-11_c4	YAG	1500	2.5 GPa	144	-15.2	*-14.6*	*-16.0*	*-16.1*	CAMECA 1280 tr.
YLPD-1_s1	YAG	1600	1 atm	24	-14.4				SHRIMP tr.

1087

s = SHRIMP, c = CAMECA IMS-1280, ns = NanoSIMS, d.p. = depth profiling, tr. = line-scan. For HP wet experiments, two sets of parameters are given depending on the position of the diffusion interface. All values in italics are those defining the two Arrhenius relationships for slow and fast mechanisms. $^{18}O_i''$ = oxygen in interstitial site, $V_O^{\bullet\bullet}$ = oxygen vacancy, $O_O^{\times}$ = oxygen in lattice site.

Experiment ID	Garnet	T (°C)	P	t (h)	$\log_{10}D$ erf fit (Eq. 1)	$\log_{10}D$ $^{18}O_i''$ diff-reac	$\log_{10}D$ $V_O^{\bullet\bullet}$ diff-reac	$\log_{10}D$ $O_O^{\times}$ diff-reac	Analytical method
YLPD-1_c1	YAG	1600	1 atm	24	-14.7				CAMECA 1280 tr.
YLPD-1_c2	YAG	1600	1 atm	24	-14.7				CAMECA 1280 tr.
YLPD-1_c3	YAG	1600	1 atm	24	-14.7				CAMECA 1280 tr.
YLPD-1_c4	YAG	1600	1 atm	24	-14.5				CAMECA 1280 tr.
YLPD-2_s1	YAG	1500	1 atm	168	-14.8				SHRIMP tr.
YLPD-2_c1	YAG	1500	1 atm	168	-15.1				CAMECA 1280 tr.
YLPD-2_c2	YAG	1500	1 atm	168	-15.0				CAMECA 1280 tr.
YLPD-2_c3	YAG	1500	1 atm	168	-15.0				CAMECA 1280 tr.
YLPD-2_c4	YAG	1500	1 atm	168	-15.1				CAMECA 1280 tr.

s = SHRIMP, c = CAMECA IMS-1280, ns = NanoSIMS, d.p. = depth profiling, tr. = line-scan. For HP wet experiments, two sets of parameters are given depending on the position of the diffusion interface. All values in italics are those defining the two Arrhenius relationships for slow and fast mechanisms. $^{18}O_i''$ = oxygen in interstitial site, $V_O^{\bullet\bullet}$ = oxygen vacancy, $O_O^{\times}$ = oxygen in lattice site.

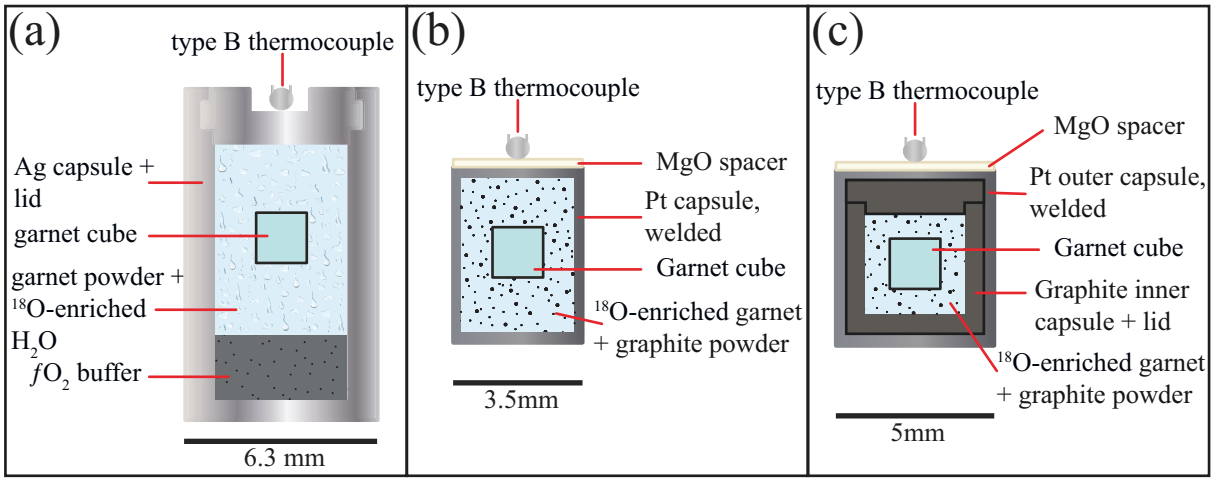
(a)
type B thermocouple
Ag capsule + lid
garnet cube
garnet powder + ^{18}O-enriched H_2O
fO_2 buffer
6.3 mm
(b)
type B thermocouple
MgO spacer
Pt capsule, welded
Garnet cube
^{18}O-enriched garnet + graphite powder
3.5mm
(c)
type B thermocouple
MgO spacer
Pt outer capsule, welded
Garnet cube
Graphite inner capsule + lid
^{18}O-enriched garnet + graphite powder
5mm

Fig. 1.

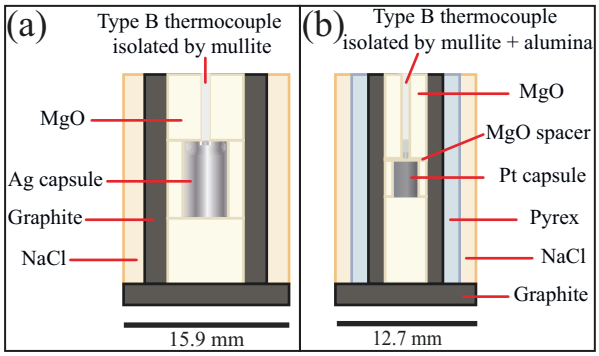
(a)
Type B thermocouple isolated by mullite
MgO
Ag capsule
Graphite
NaCl
15.9 mm
(b)
Type B thermocouple isolated by mullite + alumina
MgO
MgO spacer
Pt capsule
Pyrex
NaCl
Graphite
12.7 mm

Fig. 2.

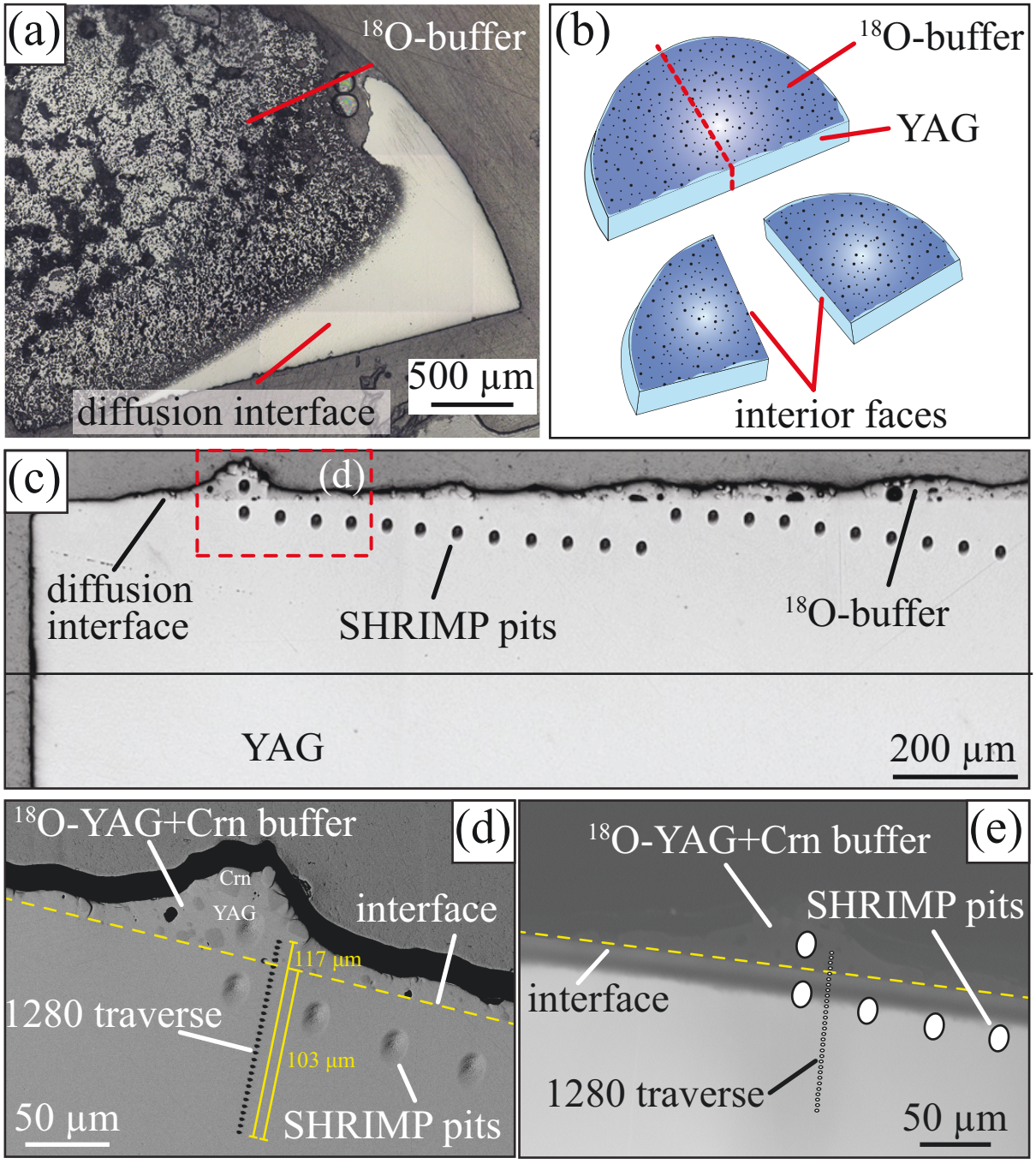
(a)
^{18}O-buffer
diffusion interface
500 µm
(b)
^{18}O-buffer
YAG
interior faces
(c)
(d)
diffusion interface
SHRIMP pits
^{18}O-buffer
YAG
200 µm
^{18}O-YAG+Crn buffer
(d)
Crn
YAG
interface
117 µm
1280 traverse
103 µm
50 µm
SHRIMP pits
^{18}O-YAG+Crn buffer
(e)
SHRIMP pits
interface
1280 traverse
50 µm

Fig. 3.

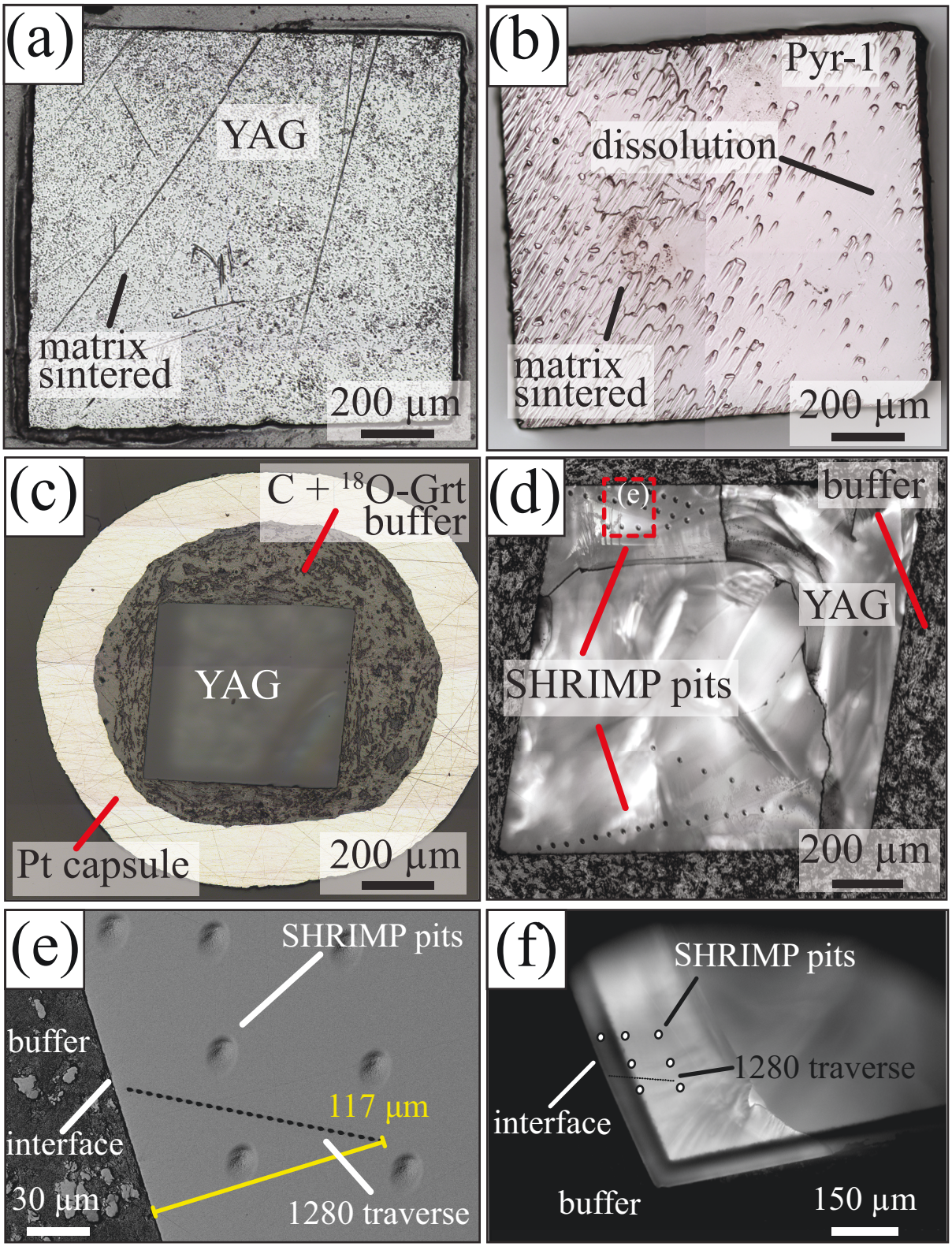
(a)
YAG
matrix
sintered
200 µm
(b)
Pyr-1
dissolution
matrix
sintered
200 µm
(c)
C + ^{18}O-Grt
buffer
YAG
Pt capsule
200 µm
(d)
(e)
buffer
YAG
SHRIMP pits
200 µm
(e)
SHRIMP pits
buffer
117 µm
interface
30 µm
1280 traverse
(f)
SHRIMP pits
1280 traverse
interface
buffer
150 µm

Fig. 4.

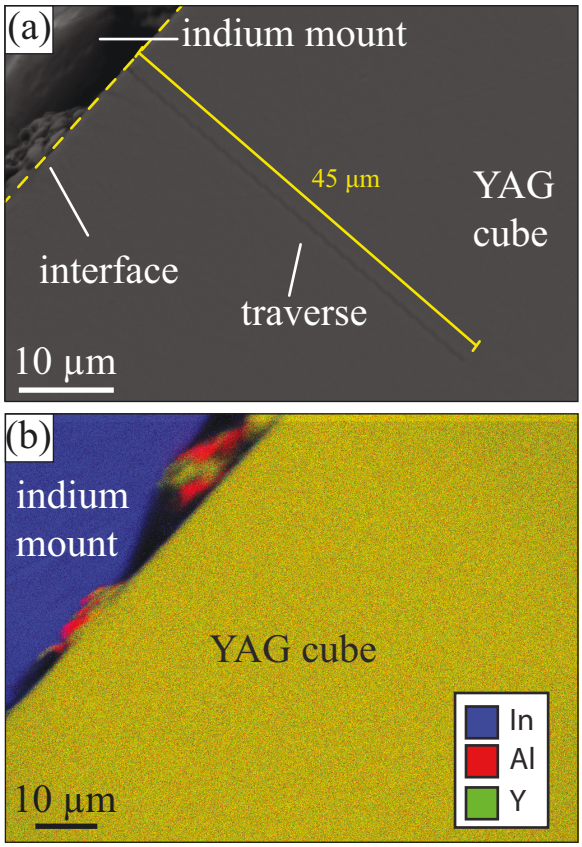
(a)
indium mount
45 µm
YAG
cube
interface
traverse
10 µm
(b)
indium
mount
YAG cube
In
Al
Y
10 µm

Fig. 5

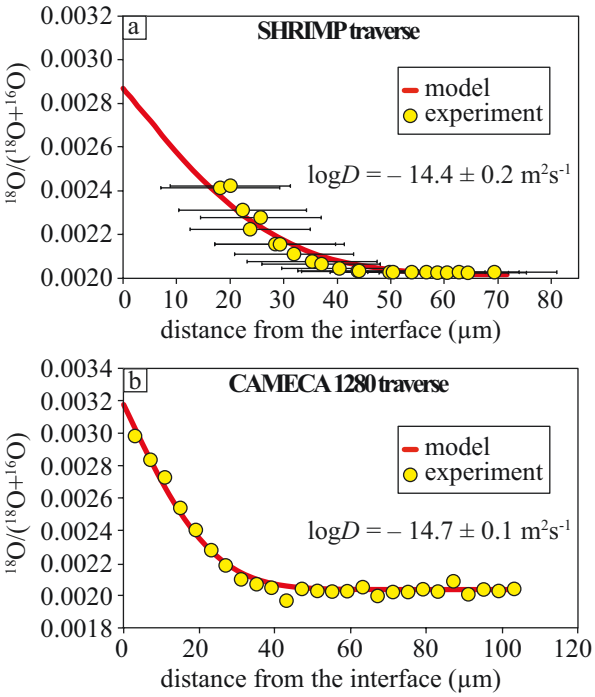
a
SHRIMP traverse
model
experiment
logD = – 14.4 ± 0.2 m²s⁻¹
0.0032
0.0030
0.0028
0.0026
0.0024
0.0022
0.0020
0 10 20 30 40 50 60 70 80
distance from the interface (μm)
b
CAMECA 1280 traverse
model
experiment
logD = – 14.7 ± 0.1 m²s⁻¹
0.0034
0.0032
0.0030
0.0028
0.0026
0.0024
0.0022
0.0020
0.0018
0 20 40 60 80 100 120
distance from the interface (μm)
18O/(18O+16O)

Fig. 6.

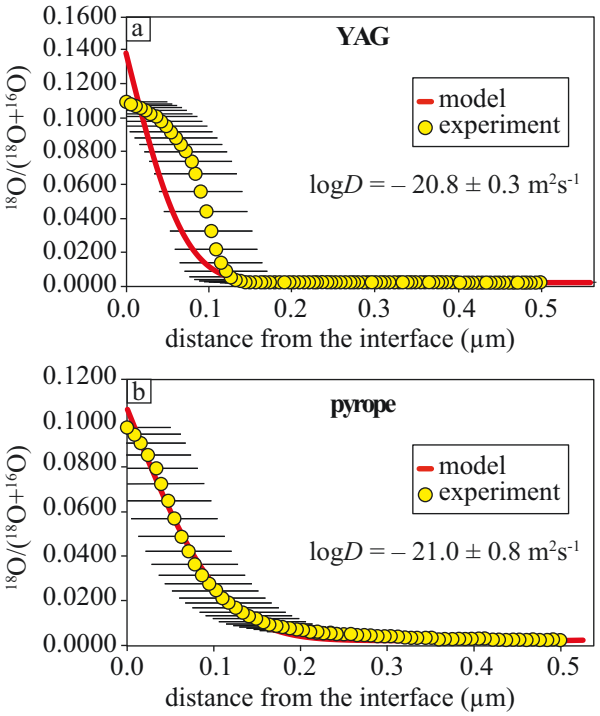
a
YAG
model
experiment
logD = – 20.8 ± 0.3 m²s⁻¹
0.1600
0.1400
0.1200
0.1000
0.0800
0.0600
0.0400
0.0200
0.0000
0.0
0.1
0.2
0.3
0.4
0.5
distance from the interface (μm)
18O/(18O+16O)
b
pyrope
model
experiment
logD = – 21.0 ± 0.8 m²s⁻¹
0.1200
0.1000
0.0800
0.0600
0.0400
0.0200
0.0000
0.0
0.1
0.2
0.3
0.4
0.5
distance from the interface (μm)
18O/(18O+16O)

Fig. 7.

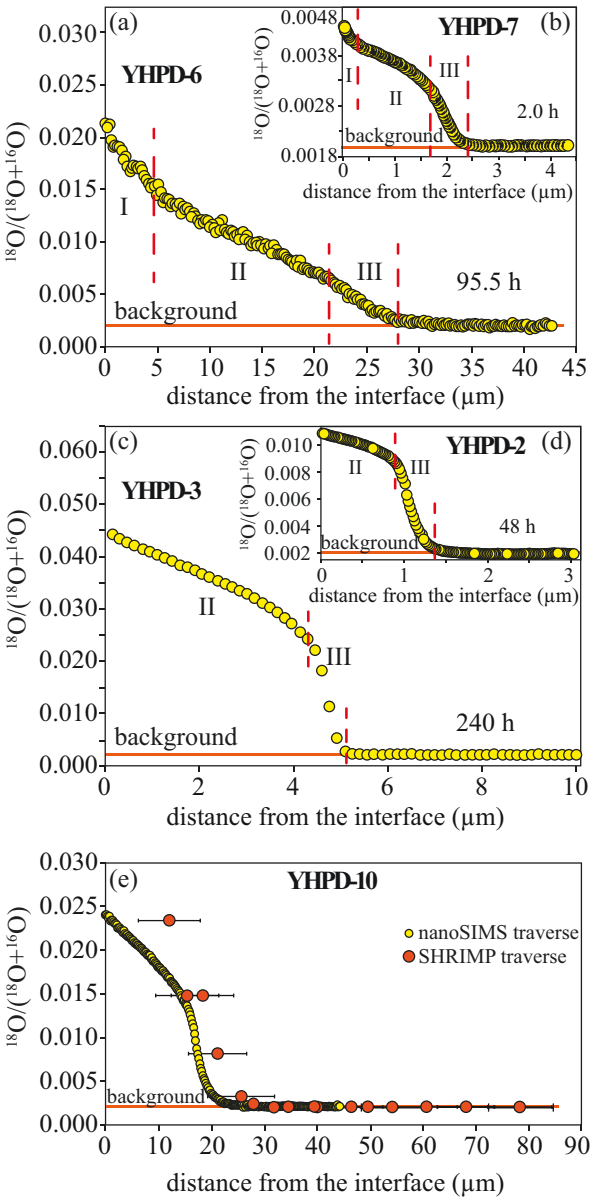
(a)
YHPD-6
(b)
YHPD-7
2.0 h
95.5 h
(c)
YHPD-3
(d)
YHPD-2
48 h
240 h
(e)
YHPD-10
nanoSIMS traverse
SHRIMP traverse
background
I
II
III
distance from the interface (μm)
18O/(18O+16O)

Fig. 8.

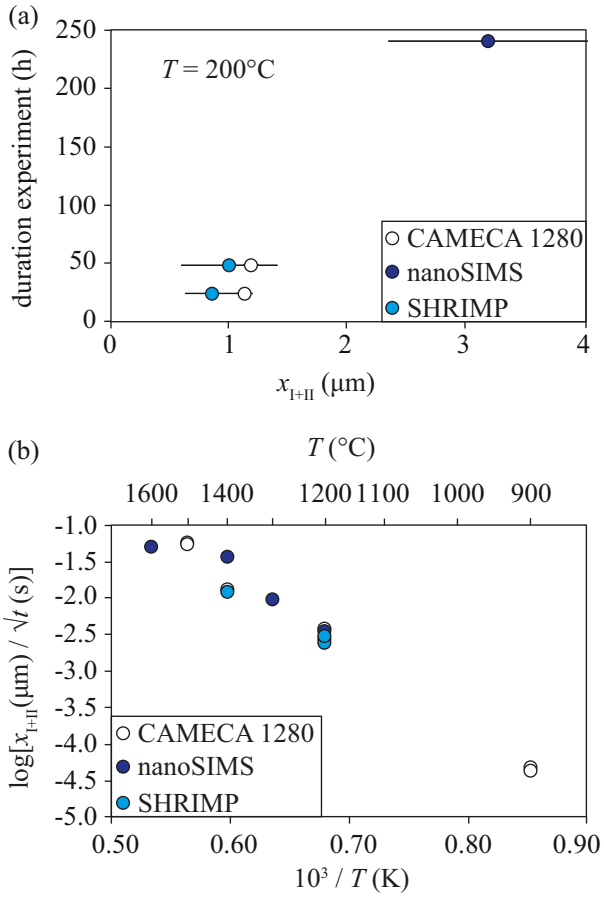
(a)
duration experiment (h)
T = 200°C
CAMECA 1280
nanoSIMS
SHRIMP
x_I+II (µm)
(b)
T (°C)
log[x_I+II(µm) / √t (s)]
CAMECA 1280
nanoSIMS
SHRIMP
10³ / T (K)

Fig. 9.

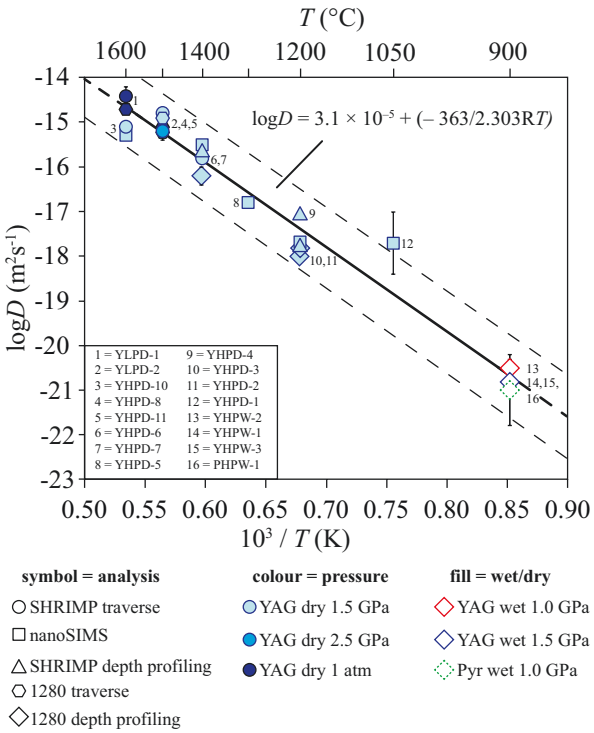
T (°C)
1600
1400
1200
1050
900
-14
-15
-16
-17
-18
-19
-20
-21
-22
-23
logD (m²s⁻¹)
logD = 3.1 × 10⁻⁵ + (– 363/2.303RT)
1
2,4,5
3
6,7
8
9
10,11
12
13
14,15,
16
1 = YLPD-1
2 = YLPD-2
3 = YHPD-10
4 = YHPD-8
5 = YHPD-11
6 = YHPD-6
7 = YHPD-7
8 = YHPD-5
9 = YHPD-4
10 = YHPD-3
11 = YHPD-2
12 = YHPD-1
13 = YHPW-2
14 = YHPW-1
15 = YHPW-3
16 = PHPW-1
0.50
0.55
0.60
0.65
0.70
0.75
0.80
0.85
0.90
10³ / T (K)
symbol = analysis
SHRIMP traverse
nanoSIMS
SHRIMP depth profiling
1280 traverse
1280 depth profiling
colour = pressure
YAG dry 1.5 GPa
YAG dry 2.5 GPa
YAG dry 1 atm
fill = wet/dry
YAG wet 1.0 GPa
YAG wet 1.5 GPa
Pyr wet 1.0 GPa

Fig. 10.

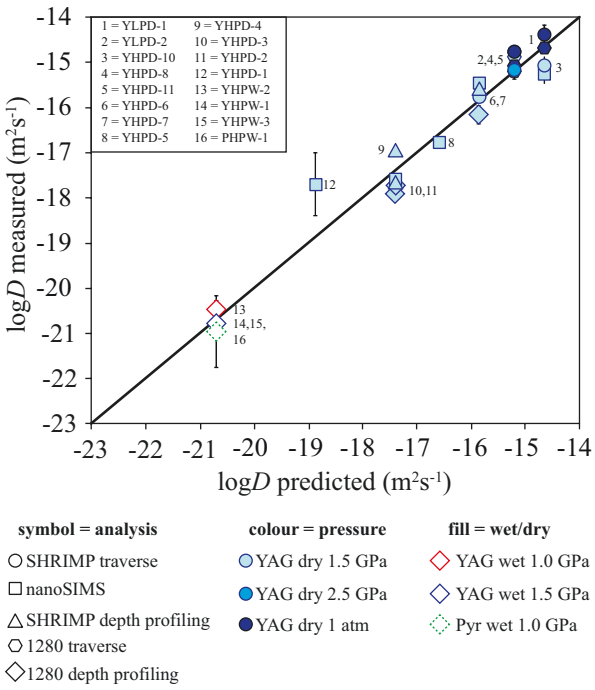
1 = YLPD-1
2 = YLPD-2
3 = YHPD-10
4 = YHPD-8
5 = YHPD-11
6 = YHPD-6
7 = YHPD-7
8 = YHPD-5
9 = YHPD-4
10 = YHPD-3
11 = YHPD-2
12 = YHPD-1
13 = YHPW-2
14 = YHPW-1
15 = YHPW-3
16 = PHPW-1
1
2,4,5
3
6,7
8
9
10,11
12
13
14,15,
16
-14
-15
-16
-17
-18
-19
-20
-21
-22
-23
logD measured (m²s⁻¹)
-23 -22 -21 -20 -19 -18 -17 -16 -15 -14
logD predicted (m²s⁻¹)

symbol = analysis
colour = pressure
fill = wet/dry
SHRIMP traverse
nanoSIMS
SHRIMP depth profiling
1280 traverse
1280 depth profiling
YAG dry 1.5 GPa
YAG dry 2.5 GPa
YAG dry 1 atm
YAG wet 1.0 GPa
YAG wet 1.5 GPa
Pyr wet 1.0 GPa

Fig. 11.

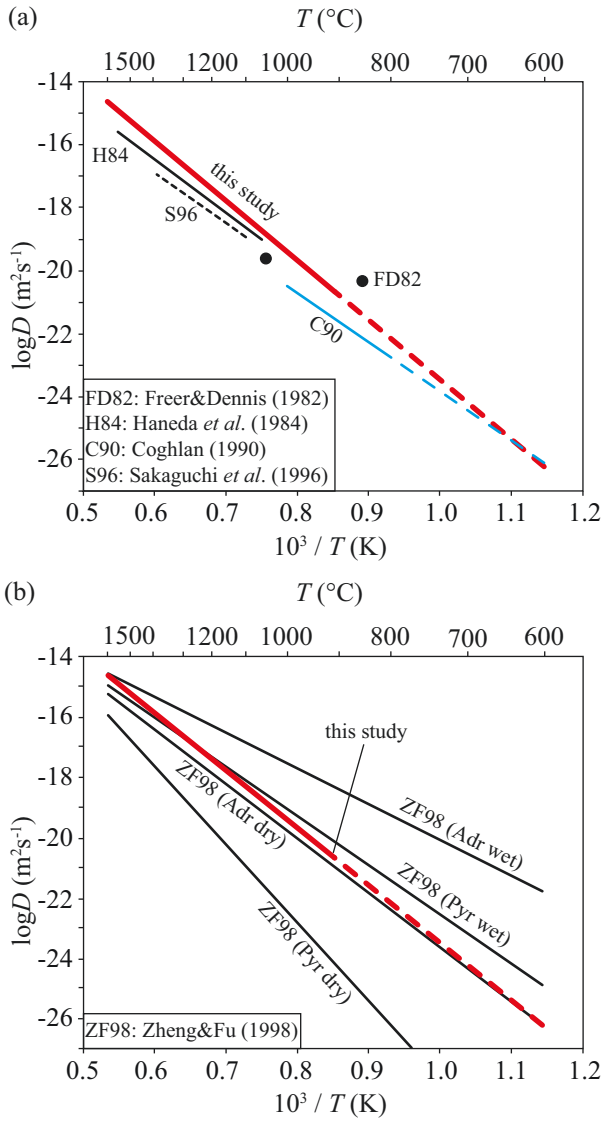
(a)
T (°C)
1500 1200 1000 800 700 600
-14 -16 -18 -20 -22 -24 -26
log D (m²s⁻¹)
H84
this study
S96
FD82
C90
FD82: Freer&Dennis (1982)
H84: Haneda et al. (1984)
C90: Coghlan (1990)
S96: Sakaguchi et al. (1996)
0.5 0.6 0.7 0.8 0.9 1.0 1.1 1.2
10³ / T (K)
(b)
T (°C)
1500 1200 1000 800 700 600
-14 -16 -18 -20 -22 -24 -26
log D (m²s⁻¹)
this study
ZF98 (Adr wet)
ZF98 (Adr dry)
ZF98 (Pyr wet)
ZF98 (Pyr dry)
ZF98: Zheng&Fu (1998)
0.5 0.6 0.7 0.8 0.9 1.0 1.1 1.2
10³ / T (K)

Fig. 12.

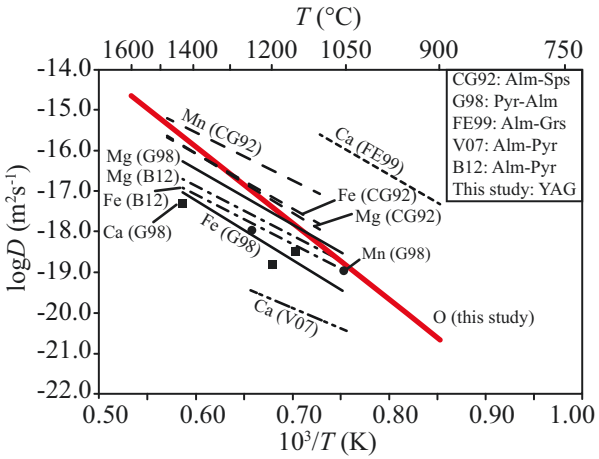
T (°C)
1600 1400 1200 1050 900 750
-14.0
-15.0
-16.0
-17.0
-18.0
-19.0
-20.0
-21.0
-22.0
logD (m²s⁻¹)
0.50 0.60 0.70 0.80 0.90 1.00
10³/T (K)
CG92: Alm-Sps
G98: Pyr-Alm
FE99: Alm-Grs
V07: Alm-Pyr
B12: Alm-Pyr
This study: YAG
Mn (CG92)
Ca (FE99)
Mg (G98)
Mg (B12)
Fe (B12)
Ca (G98)
Fe (G98)
Fe (CG92)
Mg (CG92)
Mn (G98)
Ca (V07)
O (this study)

Fig. 13.

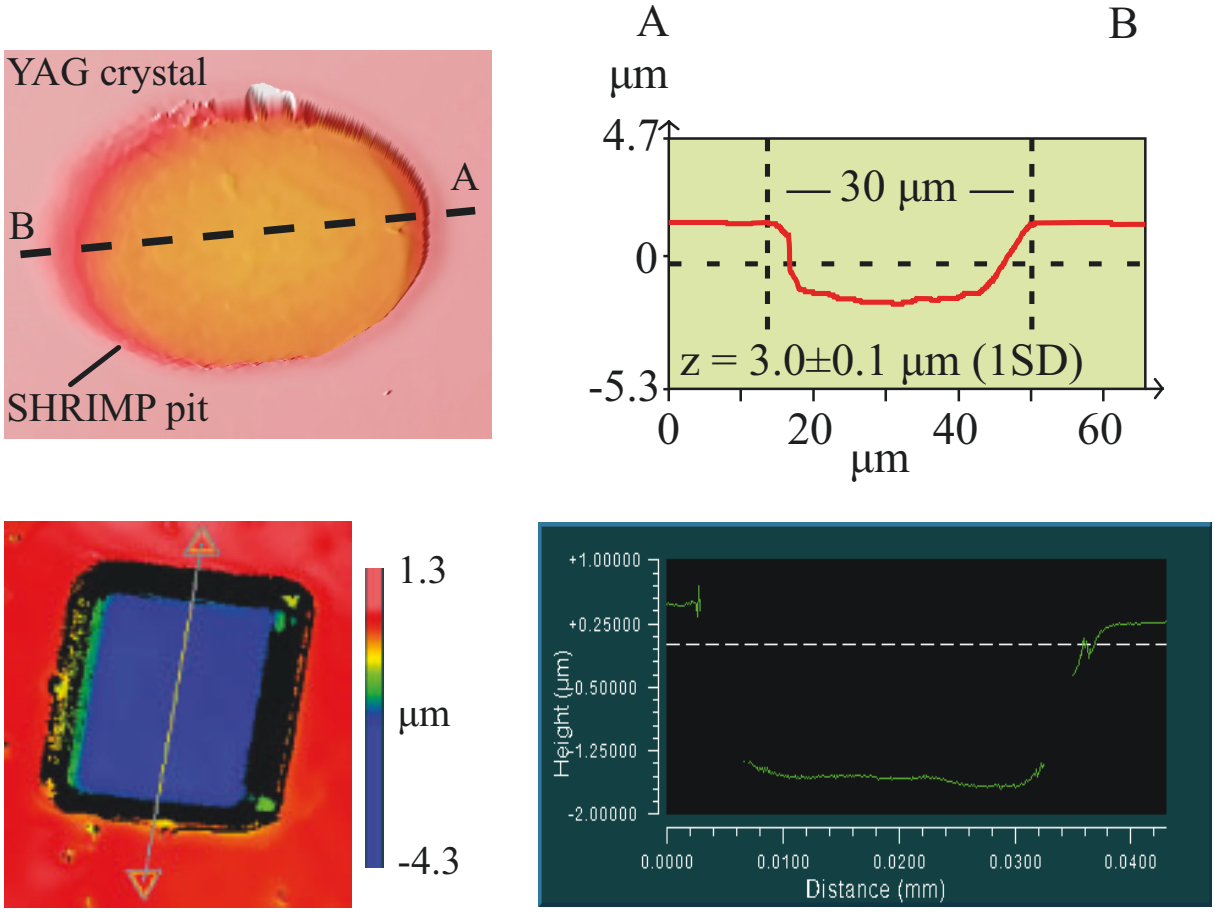
YAG crystal
A
B
SHRIMP pit
A
B
µm
4.7
0
-5.3
— 30 µm —
z = 3.0±0.1 µm (1SD)
0
20
40
60
µm
1.3
µm
-4.3
+1.00000
+0.25000
-0.50000
-1.25000
-2.00000
Height (µm)
0.0000
0.0100
0.0200
0.0300
0.0400
Distance (mm)

Fig. S1

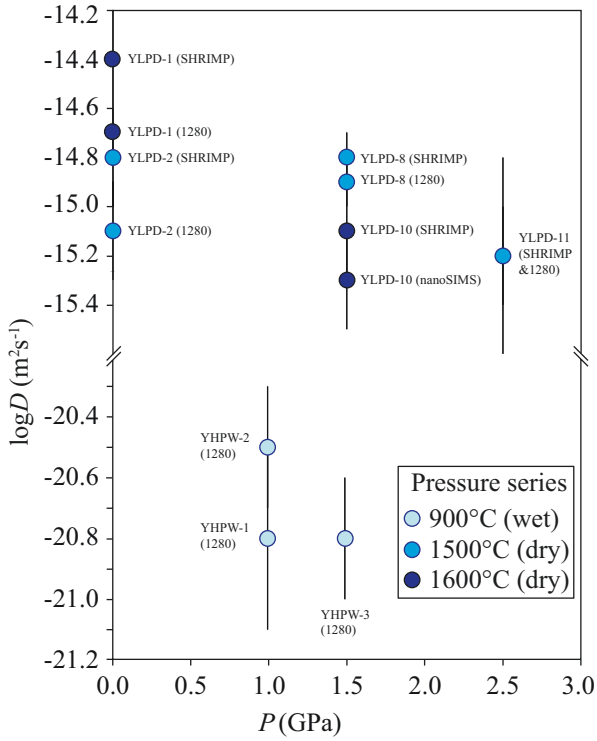
-14.2
-14.4
-14.6
-14.8
-15.0
-15.2
-15.4
-20.4
-20.6
-20.8
-21.0
-21.2
logD (m²s⁻¹)
YLPD-1 (SHRIMP)
YLPD-1 (1280)
YLPD-2 (SHRIMP)
YLPD-2 (1280)
YLPD-8 (SHRIMP)
YLPD-8 (1280)
YLPD-10 (SHRIMP)
YLPD-10 (nanoSIMS)
YLPD-11 (SHRIMP &1280)
YHPW-2 (1280)
YHPW-1 (1280)
YHPW-3 (1280)
Pressure series
900°C (wet)
1500°C (dry)
1600°C (dry)
0.0
0.5
1.0
1.5
2.0
2.5
3.0
P (GPa)

Fig. S2.